Journal Pre-proofs

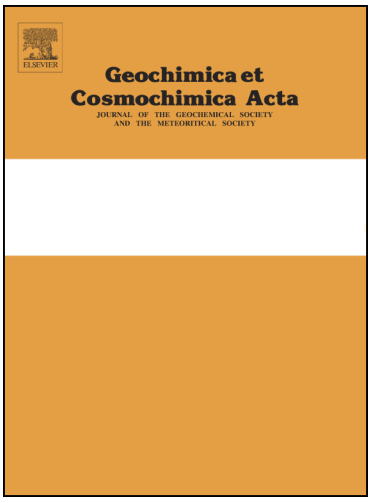

Integrated Petrological and Fe-Zn Isotopic Modelling of Plutonic Differentiation

Madeleine A. Stow, Julie Prytulak, Madeleine C. S. Humphreys, Geoffrey M. Nowell

PII: S0016-7037(21)00724-9
DOI: https://doi.org/10.1016/j.gca.2021.12.018
Reference: GCA 12491

To appear in: *Geochimica et Cosmochimica Acta*

Received Date: 16 July 2021
Revised Date: 13 December 2021
Accepted Date: 17 December 2021

Please cite this article as: Stow, M.A., Prytulak, J., C. S. Humphreys, M., Nowell, G.M., Integrated Petrological and Fe-Zn Isotopic Modelling of Plutonic Differentiation, *Geochimica et Cosmochimica Acta* (2021), doi: https://doi.org/10.1016/j.gca.2021.12.018

Integrated Petrological and Fe-Zn Isotopic Modelling of Plutonic Differentiation

Madeleine A. Stow[a*], Julie Prytulak[a], Madeleine C. S. Humphreys[a], Geoffrey M. Nowell[a]

[a] Department of Earth Sciences, Durham University, Durham, DH1 3LE, UK

* Corresponding author: Madeleine A. Stow (madeleine.a.stow@durham.ac.uk)

Abstract

The upper continental crust is formed from chemically diverse granitic plutons. Active debate surrounds the range of physical conditions (P-T-X-fO_2) and differentiation processes which occur in mush bodies that solidify to form plutons. Transition metal stable isotopes are increasingly employed to trace magmatic processes in both extrusive lavas and intrusive plutonic suites, with a focus on analysis of whole rock powders. However, studies of plutonic suites often overlook the complex textures represented within coarse grained samples, and how these will influence whole rock isotopic compositions.

Here we examine the calc-alkaline Boggy Plain Zoned Pluton, SE Australia, which closely approximates closed system behaviour during magmatic differentiation. We combine petrological examination with Fe and Zn isotopic analysis of biotite, hornblende and magnetite mineral separates and whole rock powders. Whole rock Fe isotopic composition (as $\delta^{56}Fe$) increases from 0.038‰ to 0.171‰ with decreasing MgO content, while mineral separates display heavy Fe isotope enrichment in the order magnetite > biotite = hornblende > pyroxene. A lack of correlation between whole rock Fe and Zn isotopic compositions suggests that the Fe isotopic variation is predominantly driven by closed system fractional crystallisation: specifically by the balance between crystallisation of isotopically heavy magnetite, and isotopically light silicates. To demonstrate this quantitatively, temperature dependent mineral-melt fractionation factors were derived from the mineral separate data ($\Delta^{56}Fe_{mag\text{-}melt} = 0.17x10^6/T^2$ and $\Delta^{56}Fe_{bt/hbd\text{-}melt} = -0.12x10^6/T^2$) and used to construct models that successfully reproduce the observed Fe isotopic variation during fractional crystallisation. These fractionation factors are compared to theoretical and empirical estimates from previous studies. We highlight that accurate determinations of temperature and modal mineralogy are critical when modelling Fe isotopic variations in plutonic suites. Successful interpretation of equilibrium Fe isotopic fractionation in a relatively simple calc-alkaline suite like the Boggy Plain Zoned Pluton paves the way for Fe isotopes to be used to investigate more complex mush bodies.

Keywords: crystal mush, granite, differentiation, transition metals, Fe-Zn stable isotopes

1. Introduction

It is now generally accepted that many crustal magma reservoirs are not melt-dominated systems, but instead are crystal-rich mushy regions where high melt fractions are present only transiently (e.g. Bachmann and Bergantz, 2004; Hildreth, 2004; Cashman et al., 2017; Sparks et al., 2019). The conceptual shift away from traditional melt-rich magma 'chambers' has generated new questions about storage conditions and differentiation processes in plutonic settings (e.g. Sparks et al., 2019). In melt dominated reservoirs, closed system in-situ fractional crystallisation was the intuitive differentiation mechanism to form chemically and lithologically zoned plutons (e.g. Tindle and Pearce, 1981; Wyborn et al., 1987). However, there is debate about how efficient crystal-liquid segregation processes are in evolved crystal mushes with a more viscous, low-density melt (Holness,

2018; Bachmann and Huber, 2019). Other processes such as magma recharge, mixing, assimilation and/or reactive porous flow (Jackson et al., 2018; Weinberg et al., 2021) may also be important controls on chemical variability. Despite these conceptual developments, chemical trends in plutonic suites are commonly modelled as the liquid line of descent of a liquid magma body undergoing fractional crystallisation and/or assimilation (e.g. Burton-Johnson et al., 2019), even though this may not be realistic.

The stable isotope variations of transition metals such as Fe are well established tracers of magmatic processes (e.g. see review in Dauphas et al., 2017). Equilibrium stable isotope fractionation in magmatic systems is fundamentally driven by differences in bond strength between minerals, melts and fluids. With Fe a major element constituent of melts and minerals, Fe isotopes can be a powerful tool to investigate processes such as partial melting (e.g. Williams et al., 2005; Weyer and Ionov, 2007; Williams and Bizimis, 2014; Xia et al., 2017; Xu et al., 2017), fractional crystallisation (e.g. Teng et al., 2008; Schuessler et al., 2009; Sossi et al., 2012; Du et al., 2017; He et al., 2017; Williams et al., 2018; Du et al., 2019) and fluid exsolution (e.g. Heimann et al. 2008; Telus et al., 2012). In minerals, Fe^{3+} preferentially enters tetrahedral sites whereas larger Fe^{2+} ions tend to be octahedrally coordinated. Tetrahedral Fe-O bonds are shorter and stiffer, and preferentially incorporate heavy Fe isotopes (Schauble, 2004). Variation in Fe oxidation state and coordination environment is thought to control the order of heavy Fe isotope enrichment in common rock forming minerals, such that: feldspar>magnetite> biotite, hornblende > pyroxene, olivine > ilmenite (Polyakov et al., 2007; Dauphas et al., 2012; Sossi et al., 2012; Sossi and O'Neill, 2017; Wu et al., 2017; Cao et al., 2019). In the coexisting melt, bond strength increases with $Fe^{3+}/\Sigma Fe$ ratio, and is greatest in high silica, polymerised, alkali rich melts (Dauphas et al., 2014). Fractionation factors (i.e. the difference in isotopic composition between phases) are also inversely proportional to T^2. Hence, equilibrium fractionation factors are controlled by mineral and melt chemistry, but also by intrinsic parameters such as temperature and fO_2. Taken together, this means that Fe isotopes could in principle address many important questions in petrology such as the relationship between melt redox state, crystallising assemblage and differentiation pathway. Conversely, processes such as additions of new batches of magma (Nebel et al., 2020), thermal diffusion (Zambardi et al., 2014; Gajos et al., 2016) and/or fluid exsolution (Poitrasson and Freydier, 2005; Heimann et al., 2008; Telus et al., 2012) may overprint these equilibrium isotopic fractionations.

Zinc and Fe isotopic compositions can be combined to further constrain magmatic processes and test the significance of possible overprinting processes. In contrast to Fe, Zn has relatively simple behaviour in magmatic systems (Telus et al., 2012; Moynier et al., 2017; Xia et al., 2017; McCoy-West et al., 2018). Zinc is a monovalent trace element present only as Zn^{2+}, so isotopic fractionation is not driven directly by changes in redox conditions. Numerous studies have demonstrated that negligible Zn isotope fractionation (<0.1‰) occurs during fractional crystallisation alone (Chen et al., 2013; Doucet et al., 2018; Huang et al., 2018). However, some high silica rhyolites, S-type granites and pegmatites have Zn isotopic compositions up to 0.6‰ heavier than mantle derived basalts (Telus et al., 2012; Xia et al., 2017; Doucet et al., 2018; Wang et al., 2020). Exsolution of isotopically light fluids (Telus et al., 2012; Wang et al., 2020) and/or enrichment of heavy Zn in the melt during partial melting (Doucet et al., 2018; Sossi et al., 2018a; Xu et al., 2019) are proposed to explain heavy Zn isotopic compositions in these evolved samples. Furthermore, extreme Zn isotopic compositions can be generated by chemical and/or thermal diffusion processes (e.g. McCoy-West et al., 2018).

Doucet et al. (2020) discussed the principle of the coupled isotope systematics of Fe and Zn. Theoretically, since Fe and Zn are fractionated by different processes, Fe and Zn isotopes can be decoupled by interaction with fluids or sediments, and fO_2 variations during differentiation. However, a correlation between Fe and Zn isotopes in the same samples would imply that both are fractionated by the same processes. Hence, we employ a paired Fe-Zn approach in this study in order to better identify the causes of both Fe and Zn isotope fractionation in the BPZP.

Previous work on plutonic rocks has employed the isotopic composition of homogenous whole rock powders, in the absence of key information on petrographic textures (e.g. Poitrasson and Freydier, 2005; Schoenberg and von Blanckenburg, 2006; Heimann et al., 2008; Telus et al., 2012; Foden et al., 2015; Gajos et al., 2016; He et al., 2017; Du et al., 2019; Nebel et al., 2020). These types of studies make the implicit assumption that the whole rock composition is analogous to the evolving liquid composition. This may be valid for lavas, but is less appropriate for samples from coarse-grained, texturally complex plutonic suites. Plutonic rocks are typically formed of primocrysts surrounded by interstitial phases crystallised from trapped melt, so neighbouring phases in solidified samples were not necessarily in chemical equilibrium with each other. If chemical trends are generated by fractional crystallisation, samples have also experienced some degree of crystal-melt segregation. Therefore, whole rock composition of plutonic rocks is generally not equivalent to the melt composition at the time of crystallisation (Chappell and Wyborn, 2004; Vernon and Collins, 2011; Barnes et al., 2019).

It is crucial to consider this petrographic complexity when constructing geochemical models for plutonic suites. For example, it is common practice to choose the sample with the highest MgO content as the 'parental' magma composition for fractional crystallisation models of co-genetic lava suites, or to back-calculate a 'parental' magma composition from the most mafic sample in a suite (e.g. Sossi et al., 2016). However, this approach is problematic in plutonic settings where the most MgO rich samples are cumulates which do not represent real liquid compositions. Further, the competing controls on Fe isotope fractionation are generally difficult to distinguish using whole rock analyses alone. For example, a trend to increasingly heavy Fe isotopic composition with SiO_2 content is observed in a global compilation of igneous whole rocks, irrespective of tectonic setting. This variation has been ascribed to disparate processes such as fluid exsolution (Poitrasson and Freydier, 2005; Heimann et al., 2008; Telus et al., 2012), thermal diffusion (Zambardi et al., 2014; Gajos et al., 2016), fractional crystallisation and subsequent fO_2 variations (Sossi et al., 2012; Foden et al., 2015) and changing melt structure (Dauphas et al., 2014). It is critical to incorporate petrologic information, and, wherever analytically feasible, analyse individual mineral phases to help determine the cause of isotopic variation in a suite of related rocks.

Although intermediate to silicic plutons dominate the upper continental crust, only four previous studies have reported Fe isotopic compositions of mineral separates from granitoids (Heimann et al., 2008; Sossi et al., 2012; Telus et al., 2012; Wu et al., 2017). Of these, only Sossi et al. (2012) present mineral separates from a co-genetic plutonic suite (the low fO_2, tholeiitic Red Hills intrusion, Tasmania): there, fractionation of isotopically light pyroxene initially drives the residual magma to increasingly heavy Fe isotopic values. Upon saturation of isotopically heavy magnetite, the Fe isotopic composition of the residual magma decreases. However, these results are not necessarily directly applicable to the intermediate-silicic plutons which make up the majority of the continental crust. The continental crust is dominantly formed of I-type plutons, which crystallise from high fO_2

magmas derived from igneous protoliths, and crystallise mineral assemblages dominated by phases like biotite, hornblende and magnetite (e.g. Chappell and White, 2001).

Here, we present an integrated Fe and Zn isotope investigation of mineral separates and whole rocks from the I-type Boggy Plain Zoned Pluton, SE Australia, in order to unpick the controls on transition metal isotope fractionation in hydrous granites. The Boggy Plain Zoned Pluton formed via closed system fractional crystallisation of a calc-alkaline parent magma (Wyborn, 1983; Wyborn et al., 1987; Ickert, 2010). We combine textural and petrographic examination with Fe-Zn isotopic analysis of both whole rock powders and mineral separates for the main hosts of Fe and Zn (i.e. biotite, hornblende and magnetite). We construct temperature dependent models of isotopic fractionation that also take into account the effects of variation in modal mineralogy and fractionation factors. We consider how realistic different modelling approaches are in plutonic environments and provide a framework for further modelling of Fe isotopic variations in more complex mush settings.

2. Geological Background

2.1 Boggy Plain Zoned Pluton

The Boggy Plain Zoned Pluton (BPZP) is a type example of a concentrically zoned pluton formed by closed system fractional crystallisation of a calc-alkaline magma (Wyborn, 1983; Wyborn et al., 1987; Hoskin et al., 2000; Wyborn et al., 2001; Chappell and Wyborn, 2004; Ickert, 2010; Ickert et al., 2011; Chappell et al., 2012; Park et al., 2013; Iles, 2017). The pluton outcrops over an area of 36km^2 in the northern region of the Kosciuszko batholith in the Lachlan Fold Belt, SE Australia (Figure 1A), and crystallised at 417 ± 2Ma (Ickert, 2010). The BPZP is concentrically zoned, from minor gabbroic and dioritic cumulates at the rim, through granodiorite to granite, with lithologies becoming progressively more felsic towards the centre of the pluton. The granite is cut by late-stage aplitic dykes (Wyborn, 1983; Figure 1B). Towards the centre of the pluton, there is increasing bulk rock and mineral Fe^{3+}/Fe^{2+}, decreasing proportions of ilmenite and increasing proportions of magnetite, all of which are evidence supporting an increase in magma fO_2 of >1 log unit during differentiation (Wyborn, 1983; Czamanske and Wones, 1973). Temperature estimates from two-pyroxene and biotite-apatite geothermometry give crystallisation temperatures ranging from 900 °C in the diorite to 700 °C in the felsic lithologies (Wyborn, 1983).

The continuous chemical trends in the BPZP were generated by *in situ* fractional crystallisation of a single body of intermediate magma in an upper crustal magma chamber (Wyborn, 1983; Wyborn et al., 1987). Recent isotopic studies (Nd, Hf, U-Pb, O; Ickert, 2010; Ickert et al., 2011; Iles, 2017) suggest minor amounts (10-20%) of crustal assimilation (consistent with our ancillary data, see Supplementary Information and later discussion). However, decoupling between major element and isotopic trends suggests this assimilation probably occurs prior to upper crustal magma differentiation (Ickert, 2010) which is the focus of our study. Therefore, we consider the Boggy Plain pluton to be as representative a candidate for closed system fractionation as is feasible in nature.

2.2 Whole rock chemical variations

Major and trace element compositions of whole rock samples typically show smooth, continuous trends with SiO_2 or MgO content, consistent with fractional crystallisation of a single parent magma (Wyborn, 1983; Figure 2). Whole rock concentrations of highly incompatible elements (e.g. Rb)

increase with differentiation, and concentrations of elements compatible in the crystallising bulk assemblage decrease with differentiation (e.g. Sr, compatible in plagioclase).

To understand the behaviour of Fe isotopes, the causes of variations in Fe concentration within the suite must first be understood. Variations in whole rock Fe_2O_3 and $Fe^{3+}/\Sigma Fe$ are plotted against MgO content in Figure 2. Fe_2O_3 concentrations are scattered in samples with MgO >4.5 wt.%. These higher MgO samples are petrographically identified as cumulates due to the presence of framework forming primocrysts and interstitial phases. Here "cumulate" is taken to mean that samples have experienced a concentration of crystals and/or crystal-melt segregation (e.g. Chappell and Wyborn, 2004). Therefore, the scatter in whole rock compositions of samples with MgO >4.5 wt.% is likely due to variability in the modal mineralogy and amount of trapped interstitial melt, rather than representing variation in liquid composition. For Fe_2O_3 the scatter is dictated by the proportion of interstitial magnetite, biotite and hornblende. Similar scatter is observed for TiO_2, Zn and Sr. Below 4.5 wt.% MgO, the Fe_2O_3 trend is smooth, reflecting crystallisation of magnetite, biotite and hornblende as part of the near-liquidus mineral assemblage. The whole rock compositions are therefore more representative of the fractionating magma when MgO is below 4.5 wt.%. Whole rock $Fe^{3+}/\Sigma Fe$ increases with differentiation, and together with increasing $Fe^{3+}/\Sigma Fe$ in both biotite and hornblende in more evolved samples is thought to reflect an increase in the magma fO_2 during differentiation (Wyborn, 1983).

3. Sample Selection and Petrography

Based on major and trace element variations, samples or sampling localities from Wyborn (1983) were carefully selected to represent the complete range of lithologies observed in the BPZP. Samples were either those originally collected by Wyborn (1983), or from a field campaign in 2013 that resampled the same locations from Wyborn (1983).

We examined every sample petrographically, building on observations in Wyborn (1983) and Hoskin et al. (2000). A full description of all samples is given in Table S1. Two distinct textural groups of minerals were identified, primocrysts (i.e. euhedral crystals which likely crystallised unconfined from the magma) and interstitial phases (with anhedral morphologies which crystallised in confined spaces from the interstitial melt). In the context of the stable isotopic evolution of a cogenetic suite undergoing fractional crystallisation, we assume that only primocryst crystallisation will influence the isotopic composition of the evolving residual magma. However, the modal abundance of both primocryst and interstitial phases regulates the whole rock isotopic composition.

The lithologies in the BPZP progress from gabbro to monzodiorite to granodiorite to granite (Figure 1). This is typical of a calc-alkaline differentiation sequence in showing early magnetite saturation and crystallisation of hydrous phases such as biotite and hornblende, interpreted as the result of high initial H_2O content and high fO_2 (e.g. Sisson and Grove, 1993; Zimmer et al., 2010). Gabbros and diorites form the outer rim of the pluton and are only exposed over an area of <2km^2 (Figure 1). Samples BP41 (gabbro) and BP39 (diorite) contain framework-forming primocrysts and interstitial phases, a texture typical of cumulate rocks (e.g. Irvine, 1982). In the gabbro, the main framework forming primocryst phases are plagioclase (An_{60}) (55%), clinopyroxene (15%), orthopyroxene (10%) and minor olivine (<10%) (Figure 3A). Anhedral biotite (5%) occupies interstitial sites (Figure 3B). Titanomagnetite (here referred to as magnetite) and ilmenite are rare (<1%) and found as inclusions within pyroxenes and as discrete grains associated with biotite in interstitial sites. In the diorite, the

abundance of clinopyroxene is higher, and hornblende can be found with biotite in interstitial sites and as rims surrounding pyroxene crystals (Figure 3C), suggesting that both biotite and hornblende crystallised from melt films and trapped interstitial melt. Magnetite is almost exclusively associated with biotite and is therefore interpreted as an interstitial phase.

In more evolved samples, those with >58 wt. % SiO_2 and <4.5 wt.% MgO, biotite and hornblende replace orthopyroxene and clinopyroxene as the main ferromagnesian primocryst phases. Sample BP40 (5.32 wt.% MgO) shows the transition between the two textural regimes (Figure 3D). Pyroxenes (20%) have irregular crystal habits whereas hornblende (15%) and biotite (5%) begin to show more prismatic shapes. Oxides (1%) are predominantly magnetite and exist mostly as inclusions within biotite and hornblende. Plagioclase (35%) remains a primocryst phase, and there is the first appearance of interstitial orthoclase (often poikilitic) (15%).

In the granites (BP11, BP22, BP28 and BP29; Table S1), euhedral biotite (10%) and hornblende (15%) are the main ferromagnesian primocryst phases (Figure 3E), interpreted to have fully replaced the pyroxenes. Quartz (20%), plagioclase (35%) and orthoclase (20%) are the most abundant phases. There is 1% magnetite and minor interstitial titanite (<1%).

A fine-grained aplite (BP42 and BP12) is found in the core of the pluton. Quartz, orthoclase and plagioclase make up over 95% of the modal mineralogy, with minor biotite and magnetite (<5% by volume; Figure 3F). There is no hornblende present in the aplite. Biotite commonly shows a green colour along cleavage planes from chloritization by Cl-rich fluids.

Fe-Ti oxide minerals such as titanomagnetite can host a large proportion of the Fe in the system. Low temperature oxyexsolution of titanomagnetite is common during slow cooling, resulting in exsolution of ilmenite (Frost and Lindsley, 1991). Exsolved ilmenite can occur as lamellae along {111} planes of the magnetite host (both thin trellis-type and thicker sandwich-type) or as anhedral granules on the edge of magnetite grains (Frost and Lindsley, 1991). The exchange of Fe and Ti between magnetite and ilmenite during oxyexsolution can alter the Fe isotopic composition of the oxide minerals (e.g. Dziony et al., 2014; Chen et al., 2014; Cao et al., 2019). In the mafic cumulates, there is evidence for low temperature re-equilibration of interstitial magnetite grains. Granular exsolution and trellis and sandwich exsolution lamellae of ilmenite are only present in the mafic diorites (Figure 4 A and B). In the more evolved samples, primocryst titanomagnetite only shows very fine trellis-type exsolution lamellae (Figure 4C and D). There is no variation in exsolution style with grain size. The bulk magnetite separates were handpicked from a 125-250 µm size fraction following an initial magnetic separation. This size fraction is much larger than the scale of exsolution features (Figure 4), which permits sampling of magnetite grains in bulk with their hosted ilmenite lamellae. We are therefore confident that our approach allows us to determine the isotopic composition of bulk titanomagnetite at the time of crystallisation.

4. Analytical Methods

Twelve whole rock samples, along with biotite, hornblende and magnetite mineral separates from five of the samples, were measured for Fe-Zn isotopic compositions. Biotite, hornblende and magnetite separates were chosen because they host the majority of Fe and Zn in the system, with modal proportions varying over the differentiation sequence. Mass balance calculations show that approximately 30% of total Fe is hosted in magnetite, and the remainder distributed equally between biotite and hornblende. In contrast, <5% of the total Zn is hosted in magnetite, but up to

80% is hosted in biotite. Chemical purification and isotopic analysis were conducted at the Arthur Holmes Isotope Geology Laboratory, Durham University. Iron and Zn fractions were obtained from the same digestion. This reduces the amount of material required for isotopic analyses, which is beneficial when picking mineral separates. Since Fe is present at weight percent concentrations in all rock forming minerals, and Zn is a trace element with maximum concentrations of several hundred µg/g, the Zn concentration of mineral separates and whole rock powders dictated the mass of sample required for analysis. Biotite and hornblende mineral separates have Zn concentrations from 138-292 µg/g (Wyborn, 1983). Mass balance considerations based on whole rock and mineral separate Zn concentrations in Wyborn (1983) show that magnetite should contain 50-150 µg/g Zn. Approximately 1.5 µg total Zn is required to make at least three Zn isotopic measurements. Therefore, a minimum of 10-20 mg biotite and hornblende and 30-40mg magnetite were handpicked under binocular microscope from a 125-250µm size fraction, avoiding crystal fragments containing obvious inclusions. For whole rock analyses (9-95 µg/g Zn; Wyborn, 1983), approximately 50-70 mg of powder was required. The Nd isotopic compositions of four whole rock samples were also analysed in order to verify the absence of significant crustal assimilation (Ickert, 2010), as described in Section S2 of the Supplementary Information.

4.1 Chemical isolation

Mineral separates and whole rock samples were ground to homogenous powders using a Fritsch Pulverisette 0 agate motor and ball. Whole rock powders and silicate mineral separates were dissolved in 3 ml of Teflon Distilled (TD) 29M HF and 1 ml of TD 16M HNO_3 in Savillex beakers on a hotplate at 160 °C. The magnetite separates frequently contained silicate inclusions, which potentially have distinctive Fe and Zn isotopic compositions. Therefore, magnetite samples were dissolved in 5 ml TD 6M HCl in Savillex beakers on a hotplate at 120 °C. This allowed full dissolution of the oxides, and the remaining insoluble silicates were separated by centrifugation.

Samples were refluxed in 1 ml TD 6M HCl before being loaded onto anion exchange columns containing 2 ml Bio-Rad AG1-X8 resin (200-400 mesh) following the method of Sossi et al. (2015). The resin was initially pre-cleaned by shaking with TD 6M HCl and MQ H_2O. Following this initial fines removal and pre-clean step, 20 ml of resin was further cleaned using a BioRad Econo-Pac column with 250 ml reservoir connected to a vacuum box. Cleaning involved eluting a sequence of 200 ml each of MQ H_2O, TD 3M HCl, MQ H_2O, TD 3M HNO_3, MQ H_2O. This was repeated three times. The cleaning steps were necessary to reduce Zn procedural blanks to below 20 ng total Zn.

Most matrix elements were eluted with 14 ml TD 6M HCl, followed by Fe collection in 6 ml TD 0.5M HCl, and finally Zn collection in 4 ml TD 3M HNO_3. The isolated Zn fractions were passed through the same column procedure a second time. Column yields were consistently >95% for Fe and Zn, in agreement with Sossi et al. (2015). Total procedural blanks ranged from 10-30ng for Fe and 10-20ng for Zn during the course of the study.

4.2 Isotope Ratio Measurement

Iron isotopic measurements were carried out on a Neptune MC-ICP-MS in medium resolution mode ($m/\Delta m$ ~ 6000-8000) to resolve Fe from isobaric molecular oxide and nitride interferences. Masses ^{53}Cr, ^{54}Fe, ^{56}Fe, ^{57}Fe, ^{58}Fe, ^{60}Ni and ^{61}Ni were measured on Faraday cups L4, L2, L1, C, H1, H2 and H4 respectively. ^{53}Cr was monitored in order to correct for the atomic interference of ^{54}Cr on ^{54}Fe. $10^{11}\Omega$ resistors were used on all cups with the exception of L1, where a $10^{10}\Omega$ resistor was connected

to allow measurement of >50V signals on ^{56}Fe. Standards and samples were run at a concentration of 8-10 µg/g Fe. Typical sensitivity with wet plasma in medium resolution was ~5V/ppm on ^{56}Fe using a Savillex CF50 concentric flow nebuliser with 50µl/min uptake rate connected to a Glass Expansion borosilicate glass Cinnabar microcyclonic spray chamber. An individual measurement was comprised of 1 block of 50 cycles with an integration time of 4.194s per cycle, total analysis time around 3.5 minutes. Approximately 2 µg of Fe was consumed during one analysis at a concentration of 10 µg/g. Mass bias and instrument drift was corrected by standard sample bracketing with the IRMM-014 Fe standard and/or the isotopically indistinguishable IRMM-524 standard (Craddock and Dauphas, 2011).

Iron isotopic data are reported in delta notation relative to the IRMM-014 standard, where $\delta^{X}Fe = (^{X}Fe/^{54}Fe)_{sample}/(^{X}Fe/^{54}Fe)_{IRMM\text{-}014} - 1] \times 10^3$ and X is mass 56 or 57. All samples show mass dependent behaviour (Figure 5A). Samples were measured a minimum of three times, and errors are reported as 2SD of all individual measurements of the sample. USGS reference materials GSP-2, BHVO-2 and BIR-1a were processed and analysed alongside all unknowns, giving $\delta^{56}Fe$ values within the range of previous measurements (e.g. Craddock and Dauphas, 2011; Liu et al., 2014; Table 1). Long term reproducibility for Fe isotopic measurements was ±0.050‰ (n=148, 2SD) based on measurement of an internal lab standard '*Romil Fe'* over the course of the study.

Zinc isotopic measurements were carried out on a Neptune Plus MC-ICP-MS in low resolution mode (m/Δm ~ 400). Masses ^{62}Ni, ^{63}Cu, ^{64}Zn, ^{65}Cu, ^{66}Zn, ^{67}Zn and ^{68}Zn were measured in Faraday cups L3, L2, L1, C, H1, H2 and H3 respectively, with $10^{11}\Omega$ resistors connected to all cups. ^{62}Ni was monitored to correct for the isobaric interference of ^{64}Ni on ^{64}Zn. ^{63}Cu and ^{65}Cu were used for mass bias corrections. Samples were run at concentrations of 0.750 µg/g Zn and doped with 0.375 µg/g Cu. Typical sensitivity with wet plasma was ~4V/ppm on ^{66}Zn using the same introduction setup as for Fe. Mass bias and instrument drift was corrected by a combination of external element doping with Cu, and standard sample bracketing with the AA-ETH Zn solution (Archer et al., 2017). Data in this study is reported relative to AA-ETH, where $\delta^{X}Zn = (^{X}Zn/^{64}Zn)_{sample}/(^{X}Zn/^{64}Zn)_{AA\text{-}ETH} - 1] \times 10^3$ and X is mass 66, 67 or 68. All samples show mass dependent behaviour (Figure 5B).

The AA-ETH Zn solution has an isotopic composition indistinguishable from the certified isotopic reference material IRMM-3702, while its $\delta^{66}Zn$ value is offset relative to the commonly used reference standard JMC 3-0749 L, also known as JMC Lyon Zn (Maréchal et al., 1999) by +0.28 ± 0.02‰ (Archer et al., 2017). The majority of previous studies report data relative to JMC Lyon, but the standard is no longer available. Data from this study is recast relative to JMC-Lyon for comparison, using the correction of Archer et al. (2017). The IRMM-3702 Zn standard was measured regularly throughout this study, giving an average isotopic composition of $\delta^{66}Zn_{AA\text{-}ETH} = 0.015 \pm 0.035$‰ (n=83, 2SD), in agreement with Archer et al. (2017). Several USGS reference materials were processed and analysed alongside unknowns, giving $\delta^{66}Zn$ values which agree with previous measurements (e.g. Sossi et al., 2015; Chen et al., 2015; Table 1).

5. Results

5.1. Iron isotopic data

Iron isotopic data for whole rock and mineral separates are shown in Tables 1 and 2. Major and trace element compositions for whole rocks and mineral separates are from Wyborn (1983) and are given in the Supplementary Information.

The whole rock $\delta^{56}Fe$ values vary with whole rock MgO content. $\delta^{56}Fe$ values increase from 0.038 ± 0.024‰ in the most mafic samples to a maximum value of 0.171 ± 0.032‰ at 0.52 wt.% MgO / 73.07 wt.% SiO_2 (Figure 6). This range is similar to values previously measured in other I-type granitoids, which typically show maximum $\delta^{56}Fe$ ~ 0.21‰ with differentiation (Foden et al., 2015).

5.1.1. Mineral-mineral fractionation factors

The Fe isotopic composition of the mineral separates is shown in Table 2. As expected, the mineral separates are enriched in ^{56}Fe relative to ^{54}Fe in the order magnetite > biotite = hornblende > orthopyroxene, in agreement with previous studies (e.g. Heimann et al., 2008; Sossi et al., 2012; Wu et al., 2017). This order of isotopic enrichment also supports observations from NRIXS and Mössbauer spectroscopy that β factors, and consequently $\delta^{56}Fe$ values, increase with $Fe^{3+}/\Sigma Fe$ (Polyakov and Mineev, 2000; Polyakov et al., 2007; Schoenberg et al., 2009).

The isotopically lightest mineral separate measured is the orthopyroxene, which contains octahedrally coordinated ferrous iron ($\delta^{56}Fe$ = -0.049 ± 0.011‰; n=3). Magnetite ($^{IV}Fe^{3+}\ ^{VI}(Fe^{2+},Fe^{3+})O_4$) is the isotopically heaviest mineral phase measured. Magnetite $\delta^{56}Fe$ values are approximately constant across the differentiation sequence, varying from 0.260‰ to 0.320‰. Biotite and hornblende mineral separates have $Fe^{3+}/\Sigma Fe$ and $\delta^{56}Fe$ values between these extremes, consistent with a combination of Fe^{2+} and Fe^{3+} ions typically found in VI-fold coordination (e.g. Leake et al., 1997; Rieder et al., 1998). Biotite mineral separates span a range of $\delta^{56}Fe$ from -0.009‰ to 0.124‰ and hornblende separates from -0.007‰ to 0.102‰. Biotite and hornblende have identical isotopic compositions to each other in individual samples, with an average $\Delta^{56}Fe_{bt\text{-}hbd}$ of 0.009‰. However, biotite and hornblende separates from interstitial phases have heavier isotopic composition than primocrysts.

5.2 Zinc Isotopic Data

Zinc isotopic data for whole rock and mineral separates is presented in Tables 1 and 2. The Zn isotopic data is reported relative to the AA-ETH standard (Archer et al., 2017). With the exception of aplite samples BP12 and BP42, whole rock Zn isotopic compositions fall between $\delta^{66}Zn_{AA\text{-}ETH}$ of -0.058 ± 0.017‰ and 0.073 ± 0.014‰ (Figure 7). This is comparable to whole rock samples from the Hekla cogenetic lava suite ($\delta^{66}Zn_{AA\text{-}ETH}$ of -0.06‰ to +0.05‰; Chen et al. (2013)). With the exception of the aplites, samples are all within error of the average Zn isotopic composition of mantle derived magmas from Chen et al. (2013) of $\delta^{66}Zn_{AA\text{-}ETH}$ = 0.01 ± 0.08‰.

The silicate and oxide mineral separates from samples BP41, BP39, BP22 and BP11 have isotopic compositions within error of the average isotopic composition of basaltic magmas in Chen et al. (2013). Given that Zn^{2+} (0.74Å) has a similar ionic radius to Fe^{2+} (0.78Å) (Shannon, 1976), Zn^{2+} most likely substitutes for VI-fold coordinated Fe^{2+} in biotite, hornblende and magnetite. Silicate and oxide primocrysts from the same sample have Zn isotopic compositions that are indistinguishable within error, which is consistent with these theoretical considerations of bonding environment. Xu et al. (2019) also measured identical $\delta^{66}Zn$ in biotite, hornblende and magnetite separates from one melanosome from the Dabie Orogen, central China.

However, in the aplite sample (BP42), the magnetite has an isotopic composition within error of the other separates, but the biotite has a significantly heavier $\delta^{66}Zn_{AA\text{-}ETH}$ of 0.250 ± 0.032‰. The whole rock isotopic composition plots between the isotopic composition of biotite and magnetite, at a value of 0.238 ± 0.022‰ (2SE). The other aplite sample (BP12) also has a heavy whole rock isotopic composition of $\delta^{66}Zn_{AA\text{-}ETH}$ = 0.323 ± 0.009‰.

6. Drivers of Fe-Zn isotopic variation in the Boggy Plain Zoned Pluton

Previous geochemical and petrographic work on the BPZP indicates that its evolution very closely approximates closed system fractional crystallisation (Wyborn, 1983; Wyborn, 1987; Wyborn et al., 2001). Fractional crystallisation is commonly proposed as the dominant control on Fe isotopic variation in both extrusive (e.g. Teng et al., 2008; Schuessler et al., 2009; Du et al., 2017; Xia et al., 2017) and plutonic (e.g. Telus et al., 2012; Sossi et al., 2012; Foden et al., 2015; Du et al., 2019) suites. However, Fe isotopes can be fractionated by multiple other processes, which are often difficult to distinguish using whole rock analyses alone (e.g. Soderman et al., 2020). In contrast, fractional crystallisation is thought to cause <0.1‰ Zn isotopic fractionation (e.g. Chen et al., 2013; Doucet et al., 2018; Huang et al., 2018), but there is the potential for larger magnitudes of Zn isotopic fractionation by fluid alteration (e.g. Telus et al., 2012; Wang et al., 2020). In this section we first exclude processes that do not contribute to Fe-Zn isotopic variations in the BPZP, then assess the controls on inter-mineral isotopic fractionation factors necessary for developing internally consistent, fully quantitative models of Fe isotopic variations in calc-alkaline magmas during fractional crystallisation.

6.1 Impact of crustal assimilation and fluid exsolution on Fe-Zn isotopic compositions

Although the observed isotopic variation could, in part at least, reflect source mantle heterogeneity (e.g. Williams and Bizimis, 2014; He et al., 2017; Gleeson et al., 2020) or crustal contamination (e.g. Schoenberg and von Blanckenburg, 2006; Hiebert et al., 2016), we infer that these processes have had a negligible impact on the BPZP magma. Age-corrected whole rock εNd_i measured in this study show less than 2 epsilon unit variation (Table S2; Figure S1), with values very similar to Ickert (2010) that are typical of magmas derived from an upper mantle source. The Nd isotopic data would be consistent with either the source of the BPZP being contaminated with ~10% crustal material or the parent magma from a homogenous source assimilating approximately 10% crustal material, with the exposed Ordovician-Silurian aged sedimentary country rock proposed as a possible assimilant (Ickert, 2010). However, irrespective of whether the Nd isotopic composition is inherited from a contaminated source or early assimilation of crust, the magma appears to subsequently evolve via closed system fractional crystallisation, without further assimilation. Therefore, the effect of crustal assimilation on the variation of Fe-Zn isotopic compositions within the BPZP magma is likely to be negligible.

There is variation in both Fe and Zn whole rock isotopic compositions across the BPZP differentiation sequence (Figures 6 and 7). However, for Zn, this range is exaggerated by the presence of two isotopically heavy aplite samples. The remaining whole rock samples fall within a 0.13‰ range, with similar $\delta^{66}Zn$ values to the Hekla extrusive suite (Chen et al., 2013). Biotite, hornblende and magnetite separates also fall within this range. The mafic cumulates have the lightest $\delta^{66}Zn$ values, which may be due to the accumulation of isotopically light pyroxene which hosts the majority of Zn in these samples. There is no systematic variation in whole rock $\delta^{66}Zn$ with MgO content for the

samples with <4.5 wt.% MgO, which are interpreted to be representative of evolving magma composition. This suggests that Zn isotopes are not significantly fractionated during fractional crystallisation of the BPZP, agreeing with the findings of previous studies (e.g. Chen et al., 2013; Huang et al., 2018).

The heavy Zn isotopic composition of the aplites is most likely due to fluid alteration. Zn can be mobilised as chloride complexes in magmatic fluids (e.g. Zajacz et al., 2008). Zn-chlorides are predicted to be enriched in ^{64}Zn (Fujii et al., 2014), and exsolution of isotopically light Zn bearing fluids may therefore explain the heavy Zn isotopic compositions up to $\delta^{66}Zn_{AA\text{-}ETH} = 0.60‰$ observed in some rhyolites and pegmatites (Telus et al., 2012; Xia et al., 2017; Doucet et al., 2020). Chloritized biotite present in the most felsic lithologies of the BPZP indicates the presence of Cl-rich fluids during late-stage crystallisation. Hence, the heavy $\delta^{66}Zn$ values for the aplites and the biotite separates from BP42 are most likely caused by loss of isotopically light Zn during the chloritization of the biotite grains.

Iron isotopes can also potentially be fractionated by fluids. Fluid exsolution has been invoked to explain the heavy Fe isotopic compositions of some granites and pegmatites (Poitrasson and Freydier, 2005; Heimann et al., 2008; Telus et al., 2012). Ferrous iron is predicted to complex strongly with chloride ions in magmatic fluids; the fluid should therefore be isotopically lighter than Fe^{3+} bearing silicate minerals and melt (Fujii et al., 2014). However, both aplite samples have whole rock $\delta^{56}Fe$ values similar to the other whole rock samples. Hence, we are confident that late-stage fluid exsolution or alteration has not led to fractionation of Fe isotopes in the BPZP.

In addition, there is no correlation between whole rock $\delta^{56}Fe$ and $\delta^{66}Zn$ in the BPZP (Figure S2). The existence of coupled Fe-Zn isotope signatures in cratonic and mantle samples has previously been proposed to demonstrate that Fe and Zn isotopes are fractionated by the same processes during continental crust formation (Doucet et al., 2020). However, that co-variation is likely due to initial partial melting processes, rather than fractionation during magmatic evolution. Therefore, a lack of correlation supports the interpretation that Fe and Zn are not fractionated by the same processes in the BPZP.

Having interpreted the heavy Zn isotopic signatures as a consequence of fluid alteration, and given that there is no significant variation in $\delta^{66}Zn$ in the remainder of the whole rock data, we focus only on the Fe isotopic variations in the BPZP in the following sections.

6.2 Fe isotopic fractionation during fractional crystallisation

As demonstrated above, the Fe isotopic variation in the BPZP is not significantly influenced by source heterogeneity, crustal contamination or fluid exsolution. We therefore infer that the observed trend in whole rock $\delta^{56}Fe$ is driven by fractional crystallisation. The variation in magma $\delta^{56}Fe$ during fractional crystallisation is dependent on the fractionation of Fe between the melt and the crystallising assemblage. Fractionation factors are influenced primarily by temperature, Fe oxidation state and coordination environment (Polyakov and Mineev, 2000; Polyakov et al., 2007; Dauphas et al., 2014; Sossi and O'Neill, 2017), with the nature and number of surrounding cations exerting a minor control (Rabin et al., 2021).

In order to evaluate quantitatively the isotopic fractionation resulting from fractional crystallisation, we require accurate knowledge of mineral-melt fractionation factors. For the BPZP, we specifically

require values for hydrous phases like biotite and hornblende, which host the majority of the Fe in the system. Fractionation factors can be determined experimentally (e.g. Shahar et al., 2008; Sossi and O'Neill, 2017) or empirically from mineral separates (e.g. Sossi et al., 2012; Wu et al., 2017; Ye et al., 2020; Nie et al., 2021). Alternatively, reduced partition function ratios (β factors) in relevant phases can be derived using spectroscopic techniques (e.g. Mössbauer and nuclear resonance inelastic X-ray scattering (NRIXS)), and used to theoretically determine bond force constants (<F>) and fractionation factors (e.g. Polyakov et al., 2007; Dauphas et al., 2012; Roskosz et al., 2015; Dauphas et al., 2014; Nie et al., 2021). In addition, β factors and force constants can also be obtained from first principle calculations based on density functional theory (e.g. Blanchard et al., 2009; Rabin et al., 2021).

The strength of our BPZP dataset is that we report isotopic variations in mineral separates across a single closed system differentiation sequence, for which temperature and fO_2 estimates already exist. These mineral separate data can be used to derive accurate and internally consistent mineral-mineral and mineral-melt fractionation factors, as outlined below. These are reflective of natural variation in T-X-fO_2 conditions in calc-alkaline settings and include the first measurements for biotite and hornblende across a differentiation sequence within a single cogenetic pluton.

6.3 Controls on Inter-Mineral Fractionation Factors in the BPZP

Inter-mineral fractionation factors are expressed in the form $\Delta^{56}Fe_{min\text{-}min} = A \times 10^6/T^2$. Hence, accurate crystallisation temperature estimates are critical, given the temperature dependence of fractionation ($\Delta \propto 1/T^2$; Urey, 1947; Schauble, 2004). Crystallisation temperatures can be difficult to define given the wide solidus-liquidus interval for granites, and difficulty in determining the true composition of coexisting liquids. Ickert et al. (2011) calculated zircon crystallisation temperatures between 750-850°C in all zones of the BPZP. However, given that zircon is one of the last phases to crystallise, these temperatures are not equivalent to the crystallisation temperatures of the Fe bearing primocrysts. We estimated primocryst crystallisation temperatures for the BPZP samples using multiple geothermometers (Table 3). These results indicate a 200 °C temperature range between the most primitive and evolved samples.

Biotite, hornblende and magnetite separates are divided into two textural groups: crystals with euhedral morphologies (primocrysts) assumed to crystallise from the main magma body, and anhedral crystals crystallised from trapped interstitial melt. Biotite, hornblende and magnetite are present as interstitial phases in the mafic cumulates, whereas they are primocrysts in samples with MgO <4.5 wt.%. This is important for understanding isotopic fractionation because we assume that crystallisation of primocrysts will drive changes in the composition of the residual magma, whereas crystallisation of trapped interstitial melt will only drive local changes. Additionally, interstitial phases crystallised from isolated melt pockets may not have crystallised in chemical or isotopic equilibrium with each other, or the main magma body. Thus, mineral-mineral fractionation factors for interstitial phases may not reflect isotopic equilibrium.

Since primocryst biotite and hornblende have identical isotopic compositions in individual samples, and because biotite is present over a wider SiO_2 range than hornblende in the BPZP, we focus on variations in the magnetite-biotite fractionation factor ($\Delta^{56}Fe_{mag\text{-}bt}$) and assume this to be equal to $\Delta^{56}Fe_{mag\text{-}hbd}$. Within a cogenetic suite, variations in mineral-mineral fractionation factors can be controlled by variation in mineral composition, Fe coordination environment and/or temperature

(e.g. Schauble, 2004). In the BPZP the $\Delta^{56}Fe_{mag\text{-}bt}$ increases with $Fe^{3+}/\Sigma Fe$ of biotite (values given in Wyborn, 1983), and this coincides with increasing SiO_2 content, increasing WR $Fe^{3+}/\Sigma Fe$ and decreasing crystallisation temperature (Figures 8 and 9).

Figure 9 shows the variation in $\Delta^{56}Fe_{mag\text{-}bt}$ of the BPZP samples with temperature, using the temperature estimates given in Table 3. Here we compare these values to temperature dependent biotite-magnetite fractionation factors derived by three different methods in previous studies. The red area represents the relationship derived by Ye et al. (2020) of $\Delta^{56}Fe_{mag\text{-}bt}$ = 0.28 (±0.07) x $10^6/T^2$, from measurements of biotite and magnetite separates in a banded iron formation metamorphosed at a temperature of 538 ± 39 °C. The blue and green lines show $\Delta^{56}Fe_{mag\text{-}bt}$ derived theoretically using bond force constants (<F>) obtained from NRIXS and *ab initio* studies respectively, following the method of Dauphas et al. (2014) (Equation 1).

$$\Delta^{56}Fe_{A-B} = 2853 \times \frac{< F_A > - < F_B >}{T^2} \quad [1]$$

Thus far, only Nie et al. (2021) have determined values for the bond force constant of biotite ($<F_B>$). These values are for the biotite Fe endmember annite, and were determined by both NRIXS (188 ± 16 N/m) and DFT calculations (207 N/m). There are several published values for the bond force constant of magnetite ($<F_A>$), ranging from 198 ± 15 N/m to 292 N/m (Polyakov et al., 2007; Mineev et al., 2007; Dauphas et al., 2012; Roskosz et al., 2015; Sossi and O'Neill, 2017; Rabin et al., 2021). The reason for this wide range of values is partly due to systematic variations between values derived using NRIXS, Mössbauer and *ab initio* calculations, as previously reported (e.g. Blanchard et al., 2009; Roskoz et al., 2015; Rabin et al., 2021). Hence, to accurately compare inter-mineral fractionation factors, it is more appropriate to use force constants determined by the same technique (Rabin et al., 2021), since it is the offset between, rather than the absolute force constant values, which will control the magnitude of Fe isotope fractionation.

The blue shaded area shows the $\Delta^{56}Fe_{mag\text{-}bt}$ calculated using force constants determined by NRIXS. For $<F_B>$ in this equation, we correct the value of 188 ± 16 N/m (Nie et al., 2021) for the Fe^{3+} content on the BPZP biotite ($Fe^{3+}/\Sigma Fe$ ~ 0.18; Wyborn, 1983) as described in Nie et al. (2021), giving a value of 172 ± 16N/m. For consistency, we also chose a value for magnetite ($<F_A>$) determined by NRIXS using the same analytical and processing procedures. Dauphas et al. (2012) and Polyakov et al. (2007) derived values of 230 ± 6 N/m and 228 ± 15 N/m respectively for the magnetite force constant. However, this data was collected over a smaller energy range than in more recent studies, which may have led to underestimation of <F> (Roskosz et al., 2015). Therefore, we chose to use the value of 264 ± 6 N/m for magnetite, derived from a regression of Al-bearing spinel (Roskosz et al., 2015).

The green shaded area shows $\Delta^{56}Fe_{mag\text{-}bt}$ calculated using force constants determined from *ab initio* calculations. Errors for force constants derived through *ab initio* calculations are thought to be on the order of ±5% (Rabin et al., 2021). The value of 207 N/m is used for biotite (Nie et al., 2021). Choosing an appropriate value for magnetite is more difficult, because the two studies which give *ab initio* values for the force constants of magnetite and ulvöspinel use different calculation approaches, resulting in different force constant values (292 N/m and 207.5 N/m for magnetite and 215 N/m and 151.8 N/m for ulvöspinel respectively; Sossi and O'Neill, 2017 and Rabin et al., 2021). However, the force constant for magnetite of 207.5 N/m from Rabin et al. (2021) is identical to that

of biotite from Nie et al. (2021). Given the large $\Delta^{56}Fe_{mag\text{-}bt}$ measured in the BPZP mineral separates, and difference in valence state and coordination environment between the two phases, it is unlikely that the force constants for biotite and magnetite are the same. Instead, this is likely an artifact of differences in the calculation method used. Hence, we chose to use the value of 292 N/m from Sossi and O'Neill (2017) for magnetite. To further support this choice, Nie et al. (2021) and Sossi and O'Neill (2017) calculate similar values for fayalite (178 N/m and 144 N/m) compared to the lower value of 99.6 N/m in Rabin et al. (2021), so the two studies are more directly comparable. We also chose to use values for magnetite rather than ulvöspinel, given the low Ti content of the BPZP magnetite (<0.7 wt.% TiO_2; Wyborn, 1983).

It is remarkable that an expression describing variation in $\Delta^{56}Fe_{mag\text{-}bt}$ with temperature, determined from ironstones metamorphosed <550 °C (red line), coincides with values for biotite and magnetite crystallising from the BPZP magma when extrapolated to temperatures >690°C. These samples have experienced vastly different P-T-X-fO_2 conditions throughout their formation; for example, the biotite separates have different $Fe^{3+}/\Sigma Fe$ content: 0.13-0.22 for the BPZP (Wyborn, 1983) and 0.26-0.31 for the metamorphosed ironstone (Ye et al., 2020). The fractionation factors obtained from NRIXS data and *ab initio* calculations (blue and green lines) also show good agreement with the BPZP data. These findings demonstrate that temperature has a critical control on inter-mineral fractionation factors, in addition to variations in chemistry and/or fO_2. This highlights that accurate temperature estimates are essential when modelling Fe isotopic fractionation, especially in plutonic settings where temperature variations can be large.

7. Modelling Fe isotopic variations in plutonic settings

In this section, we use our petrographic observations and mineral separate data to produce accurate and internally consistent models of Fe isotopic fractionation during fractional crystallisation of the BPZP. The whole rock samples with MgO > 4.5 wt.% consist of accumulated crystals and variable proportions of trapped interstitial melt, thus do not approximate a true melt composition. Hence, we chose to model only the $\delta^{56}Fe$ evolution of the BPZP below 4.5 wt% MgO. From this point, whole rock isotopic composition approximates evolving magma composition. The mineral-mineral fractionation factors defined above are used to mathematically derive mineral-melt fractionation factors ($\Delta^{56}Fe_{min\text{-}melt}$). Fractional crystallisation is modelled incrementally using the Rayleigh equation (Equation 2, after Sossi et al. (2012)) as the amount of residual Fe (*f*Fe) in the system decreases:

$$\delta^{56}Fe = \delta^{56}Fe_{initial} + (\Delta^{56}Fe_{min\text{-}melt} \times \ln fFe) \quad [2]$$

For this calculation, the Fe isotopic composition of the parent magma ($\delta^{56}Fe_{initial}$) must be known, and a bulk mineral-melt fractionation factor ($\Delta^{56}Fe_{min\text{-}melt}$) and fraction of Fe remaining (*f*Fe) estimated for each model step. A series of models was produced to demonstrate how variations in modelling approaches, specifically estimates of mineral-melt fractionation factors, predict vastly different $\delta^{56}Fe$ trends in the residual magma.

7.1 Step 1: Estimating initial magma composition ($\delta^{56}Fe_{initial}$)

In lavas, the $\delta^{56}Fe$ of the most mafic sample is typically used to represent the isotopic composition of the parental magma ($\delta^{56}Fe_{initial}$). However, in plutonic settings like the BPZP, the most mafic samples are often cumulates (e.g. Chappell and Wyborn, 2004). The average $\delta^{56}Fe$ value of the mafic cumulates is 0.065‰. However, this value is most likely to reflect accumulation of isotopically light

pyroxene, rather than reflect a primary melt composition. We therefore take the parental magma to be the most mafic granodiorite containing both primocryst biotite and hornblende (BP26; $\delta^{56}Fe$ = 0.092‰), as this is assumed to be more representative of a liquid composition. Alternatively, if we assume that the interstitial biotite and hornblende in the mafic cumulates crystallised from trapped interstitial melt, it would also be appropriate to use the average isotopic composition of these interstitial phases (0.107 ± 0.030‰) as the parental melt composition.

7.2 Step 2: Estimating fraction of Fe remaining (*f*Fe)

To estimate the fraction of Fe remaining (*f*Fe), we calculate the Fe content of the evolving magma (C) using Equation 3, where C_0 is the initial FeO_{tot} concentration, F is the melt fraction, and D is the bulk mineral-melt partition coefficient for Fe.

$$C = C_0 \times F^{D-1} \quad [3]$$

The bulk partition coefficient for Fe was defined by modelling the major element trends for the BPZP whole rocks (e.g. MgO and FeO_{tot}) and selecting a bulk partition coefficient value which best reproduces the whole rock compositions (D_{MgO} =2 and D_{FeOtot} = 1.8). The model was carried out over twenty steps, as F was varied in increments of 0.05. The fraction of Fe remaining at each model step is then calculated by *f*(Fe) = (F x C)/C_0.

7.3 Step 3: Calculating mineral-melt fractionation factors

Inter-mineral fractionation factors determined directly from measurements of mineral separates (Section 6.3) are not directly used when modelling Fe isotopic evolution of a magma. Instead, mineral-melt fractionation factors are necessary to describe isotopic fractionation between the crystals and residual melt. Temperature dependent mineral-melt fractionation factors can be estimated using the Rayleigh equation (Equation 2), by iteratively selecting the $\Delta^{56}Fe_{min\text{-}melt}$ value which best fits the data (e.g. Sossi et al., 2012). Many studies use this method to estimate the bulk $\Delta^{56}Fe_{min\text{-}melt}$ which describes the entire isotopic evolution of the system rather than estimate mineral-melt fractionation factors for specific phases. For the BPZP, a bulk $\Delta^{56}Fe_{min\text{-}melt}$ of approximately -0.03‰ can describe the Fe isotopic evolution of the residual melt until 2% Fe remains (Figure 10). However, this value does not capture the true variations in the mineral assemblage during the fractionation sequence.

However, a strength of the BPZP data set is that temperature dependent fractionation factors for all the individual phases in the fractionating assemblage can be calculated using the mineral separate data. Fractionation factors for each mineral are expressed in the form $\Delta^{56}Fe_{min\text{-}melt} = A \times 10^6/T^2$.

The bulk mineral-melt fractionation factor can be expressed by weighting (W) the fractionation factors for each mineral phase (p) by their Fe content ($[FeO_{tot}]$) and modal abundance (M).

$$\text{Bulk } \Delta^{56}Fe_{min\text{-}melt} = \Sigma(\Delta^{56}Fe^{p}_{min\text{-}melt} \times W^{p}) \quad [4]$$

$$\text{where } W^{p} = (M^{p} \times [FeO_{tot}]^{p})/\Sigma(M^{p} \times [FeO_{tot}]^{p}) \quad [5]$$

For the BPZP, this gives the expression:

$$\text{Bulk } \Delta^{56}Fe_{min\text{-}melt} = (\Delta^{56}Fe_{mag\text{-}melt} \times W_{mag}) + (\Delta^{56}Fe_{bt\text{-}melt} \times W_{bt}) + (\Delta^{56}Fe_{hbd\text{-}melt} \times W_{hbd}) \quad [6]$$

Biotite and hornblende have identical isotopic composition to each other across the differentiation sequence, so $\Delta^{56}Fe_{bt\text{-}melt} = \Delta^{56}Fe_{hbd\text{-}melt}$.

$$\text{Bulk } \Delta^{56}Fe_{min\text{-}melt} = (\Delta^{56}Fe_{mag\text{-}melt} \times W_{mag}) + (\Delta^{56}Fe_{bt\text{-}melt} \times W_{bt}) + (\Delta^{56}Fe_{bt\text{-}melt} \times W_{hbd}) \quad [7]$$

The expression can therefore be expressed in terms of the relative weighting of silicate ($W_{sil} = W_{bt} + W_{hbd}$) and oxide phases ($W_{mag}$).

$$\text{Bulk } \Delta^{56}Fe_{min\text{-}melt} = (\Delta^{56}Fe_{mag\text{-}melt} \times W_{mag}) + (\Delta^{56}Fe_{bt\text{-}melt} \times W_{sil}) \quad [8]$$

For the BPZP, considerations of the modal abundances and FeO_{tot} concentrations of the fractionating assemblage show that $W_{sil} \sim 0.72$ and $W_{mag} \sim 0.28$ until 20% Fe remains. Therefore, $W_{sil} \sim 2.6 \times W_{mag}$.

$$\text{Bulk } \Delta^{56}Fe_{min\text{-}melt} = W_{mag} (\Delta^{56}Fe_{mag\text{-}melt} + 2.6\Delta^{56}Fe_{bt\text{-}melt}) \quad [9]$$

Substituting in the Bulk $\Delta^{56}Fe$ value of -0.03‰ obtained from Equation 2 (Figure 10), and the W_{mag} - value of 0.28 gives the equation:

$$-0.107 = \Delta^{56}Fe_{mag\text{-}melt} + 2.6\Delta^{56}Fe_{bt\text{-}melt} \quad [10]$$

A second equation can be generated using the mineral separate data. Since at equilibrium, $\Delta_{a\text{-}c} = \Delta_{a\text{-}b} + \Delta_{b\text{-}c}$, then for the BPZP we can express the biotite-magnetite fractionation factor as:

$$\Delta^{56}Fe_{mag\text{-}bt} = \Delta^{56}Fe_{mag\text{-}melt} + \Delta^{56}Fe_{melt\text{-}bt} \quad [11]$$

This can be rearranged to:

$$\Delta^{56}Fe_{mag\text{-}bt} = \Delta^{56}Fe_{mag\text{-}melt} - \Delta^{56}Fe_{bt\text{-}melt} \quad [12]$$

Thus, using the magnetite-biotite fractionation factors at known temperatures (Figure 9), we can then solve the values of $\Delta^{56}Fe_{mag\text{-}melt}$ and $\Delta^{56}Fe_{bt\text{-}melt}$ simultaneously, using Equations 10 and 12. The following values are calculated using the $\Delta^{56}Fe_{mag\text{-}bt}$ values for BP22, BP11 and BP42. A conservative error estimate is ±0.03‰, which is the average of the 2SD values reported for whole rock and mineral separate measurements.

- $\Delta^{56}Fe_{bt/hbd\text{-}melt} = -0.12 \times 10^6/T^2$ [13]
- $\Delta^{56}Fe_{mag\text{-}melt} = +0.17 \times 10^6/T^2$ [14]

The fractionation factors derived here do not explicitly consider the possible change in the bond force constant of ferrous iron in high silica melts (Dauphas et al., 2014), or variation in fractionation factor with mineral and melt chemistry. However, they are representative of T-fO_2 conditions in a calc-alkaline suite.

The only silicate mineral-melt fractionation factors for comparison are those from Sossi et al. (2012) for the tholeiitic Red Hills plutonic suite. Sossi et al. (2012) give a $\Delta^{56}Fe_{px\text{-}melt}$ value of $-0.17 \times 10^6/T^2$. The biotite-melt and hornblende-melt fractionation factors derived here are smaller ($\Delta^{56}Fe_{bt/hbd\text{-}melt} = -0.12 \times 10^6/T^2$). This supports theoretical considerations of valence and coordination environment. Biotite, hornblende and pyroxene all contain Fe in VI-fold coordination. However, the hydrous

silicates have higher $Fe^{3+}/\Sigma Fe$. Therefore, Fe-O bonds should be stronger in hydrous silicates than pyroxenes, and thus there should be a smaller isotopic offset between hydrous silicates and coexisting melt at equilibrium. Additionally, the $\Delta^{56}Fe_{bt/hbd\text{-}melt}$ expression is similar to a $\Delta^{56}Fe_{bt\text{-}melt}$ value of -0.1‰ estimated from measurements of biotite separates and whole rock powders in Du et al. (2017).

Perhaps surprisingly, the $\Delta^{56}Fe_{mag\text{-}melt}$ value calculated for the BPZP is within error of the value of Sossi et al. (2012) for the Red Hills suite (+0.13 x $10^6/T^2$). Magma fO_2 in the calc-alkaline BPZP suite is higher than in the tholeiitic Red Hills suite (Wyborn, 1983; Sossi et al., 2012). Theoretically, differences in melt $Fe^{3+}/\Sigma Fe$ and subsequent variation in primary magnetite composition should lead to variation in $\Delta^{56}Fe_{mag\text{-}melt}$ values between the BPZP and Red Hills. The fact that $\Delta^{56}Fe_{mag\text{-}melt}$ values are within error in both suites suggest that bonding environment and temperature exert a more dominant control on Fe isotopic fractionation factors than melt redox state.

7.4 Step 4: Deriving a bulk mineral-melt fractionation factor ($\Delta^{56}Fe_{min\text{-}melt}$)

Deriving a bulk mineral-melt fractionation factor ($\Delta^{56}Fe_{min\text{-}melt}$, Equation 4) requires knowledge of the fractionating mineral assemblage. The variation in modal proportions of the fractionating assemblage over the differentiation sequence was approximated using a linear regression of the modal abundance of primocryst phases against sample MgO content. A bulk $\Delta^{56}Fe_{min\text{-}melt}$ value is then derived at each model step by multiplying the mineral-melt fractionation factors by a Fe weighting factor for each phase (Equations 4 and 5). We use the mineral-melt fractionation factors calculated above for biotite, hornblende and magnetite, and the value of $\Delta^{56}Fe_{px\text{-}melt}$ = -0.17 x $10^6/T^2$ for pyroxene, from Sossi et al. (2012). Temperature estimates were calculated based on a linear regression of the temperature estimates for the BPZP samples (Table 3) against MgO content.

The parameters discussed above were used to model the $\delta^{56}Fe$ of the residual magma using the Rayleigh equation (Equation 2). Calculated magma $\delta^{56}Fe$ is shown by the black solid line in Figure 11. The blue shaded area shows the range in magma $\delta^{56}Fe$ when uncertainties of ±0.03‰ for the mineral-melt fractionation factors are considered. We consider this level of uncertainty to be intrinsic to such modelling and emphasise that errors in fractionation factors will always be amplified in the most silicic samples.

7.5 Model Comparisons

Several studies use the thermodynamic modelling software Rhyolite-MELTS (Gualda et al., 2012; Ghiorso and Gualda, 2015) to model variation in Fe isotopic composition during fractional crystallisation (e.g. Dauphas et al., 2014; Foden et al., 2015; He et al., 2017; Xia et al., 2017). However, MELTS cannot accurately reproduce the stability of hydrous silicates like biotite and hornblende in calc-alkaline magmas (Gualda et al., 2012). Given that these are the main Fe bearing silicate phases in the BPZP and similar systems, the evolving magma chemistry and Fe isotopic composition cannot be accurately modelled this way (See Section 4 in Supplementary Information and Figures S3 and S4). We therefore recommend that for I-type granites, modal abundances of the fractionating assemblage should be determined from petrographic observations, considering only the modal proportions of primocrysts and not interstitial phases. However, the choice of selected fractionation factors remains important.

Model 1 (Figure 11) uses the fractionation factors calculated in this study (Equations 13 and 14). For the first part of the differentiation sequence, isotopically light phases like biotite and hornblende host the majority of Fe in the system, causing an increase in the $\delta^{56}Fe$ of the evolving magma. However, below 1 wt.% MgO, when fFe < 0.1, magnetite becomes the dominant Fe host and causes a decrease in $\delta^{56}Fe$ of the most silicic magma.

In contrast, using fractionation factors for the tholeiitic Red Hills complex ($\Delta^{56}Fe_{mag\text{-}melt}$ = +0.13 x $10^6/T^2$ and $\Delta^{56}Fe_{min\text{-}melt}$ = -0.17 x $10^6/T^2$ for all silicate phases; Sossi et al., 2012), generates bulk $\Delta^{56}Fe_{min\text{-}melt}$ values of approximately -0.09‰ (Model 2; Figure 11). The calculated increase in magma $\delta^{56}Fe$ in Model 2 is therefore larger than Model 1 and does not match the BPZP whole rock data. This reinforces the notion that fractionation factors for anhydrous silicates from a tholeiitic suite are not applicable to calc-alkaline settings where hydrous phases like biotite and hornblende are present.

Finally, we calculated fractionation factors using bond force constants (Model 3; Figure 11). An average force constant (<F>) was calculated for the melt and minerals at each step of the model, following the method in Dauphas et al. (2014). Given the scarcity of force constant measurements for biotite and hornblende, <F> values for silicate minerals were calculated as in Dauphas et al. (2014): a force constant for each mineral was calculated by weighting the force constants for ferrous (197N/m) and ferric (255N/m) Fe in olivine and glasses by mineral $Fe^{3+}/\Sigma Fe$. For example, biotite with a $Fe^{3+}/\Sigma Fe$ of 0.18 has a calculated <F> of 207N/m. For magnetite, a force constant of 264 ± 6 N/m was adopted, the value determined by Roskosz et al. (2015). The bulk force constant for the minerals (<F_{min}>) was calculated by multiplying the force constants for each phase by their Fe weighting (Equation 5). For the melt, the force constant for Fe^{2+} was calculated from F^{Fe2+}=199+41/(1+$e^{34\text{-}SiO2/2}$), and Fe^{3+} assigned a value of 351N/m (Dauphas et al., 2014). <F_{melt}> was then calculated by weighting these force constants by the $Fe^{3+}/\Sigma Fe$ of the melt. Bulk $\Delta^{56}Fe_{min\text{-}melt}$ was then calculated using Equation 1. The bulk $\Delta^{56}Fe_{min\text{-}melt}$ values calculated in this way (Model 3) are always negative. This is because the force constant estimates for Fe-O bonds in the melt (351N/m for Fe^{3+} and between 200-240 N/m for Fe^{2+}) are always larger than in minerals. The bulk mineral-melt fractionation factor becomes more negative as the bond force constant of Fe^{2+} increases at high silica content (Dauphas et al., 2014), which drives an increase in $\delta^{56}Fe$ of the melt at more felsic compositions. However, the BPZP whole rock samples do not show this magnitude of $\delta^{56}Fe$ increase during differentiation. This suggests that there are uncertainties with extrapolating bond force constants measured in orthosilicates and glasses (Dauphas et al., 2014) to Fe^{3+} bearing silicates with more complex structures, like biotite and hornblende. This is demonstrated by the discrepancy between the bond force constant measured directly in biotite Fe endmember annite by NRIXS (188±16N/m at $Fe^{3+}/\Sigma Fe$ = 0.32; Nie et al., 2021) and that calculated based on biotite $Fe^{3+}/\Sigma Fe$ content as above (216N/m at $Fe^{3+}/\Sigma Fe$ = 0.32). Additionally, this approach also assumes that force constants only vary with mineral $Fe^{3+}/\Sigma Fe$. However, variation in mineral composition and/or subsequent changes in Fe-O bond length will also affect force constants (Roskosz et al., 2015; Sossi and O'Neill, 2017; Rabin et al., 2021). Therefore, further work is needed to define force constants in hydrous silicates in order to accurately model fractional crystallisation in hydrous, I-type magmas in this way.

We conclude that there are several requirements for accurate modelling of Fe isotopic evolution in co-genetic plutonic settings, which differ from modelling of co-genetic extrusive lavas.

1. Accurate modal abundances. Only the modal abundance of primocryst phases crystallising from the main magma body will influence magma $\delta^{56}Fe$ and Fe content. Interstitial phases crystallised from trapped melt will influence bulk rock $\delta^{56}Fe$ but not magma $\delta^{56}Fe$ evolution. Modal abundance estimates from observations of samples are more accurate than those estimated from Rhyolite-MELTS, especially in I-type systems.
2. Accurate estimation of parental melt composition. In contrast to extrusive suites, the most mafic samples in plutonic bodies are often cumulates and do not reflect a true liquid or parental melt composition, so should not be used as such.
3. Temperature dependent mineral-melt fractionation factors. The use of temperature dependent fractionation factors is vital in plutonic settings where temperature variations can be large. It must also be considered that fractionation factors derived from *ab initio* calculations or NRIXS studies are not necessarily directly applicable to the specific chemistry and $Fe^{3+}/\Sigma Fe$ of the minerals in the suite being studied. Therefore, empirically derived fractionation factors at similar X-fO_2 conditions may be more appropriate.

Rayleigh models like those above assume perfect closed system fractional crystallisation. Although in practice the differentiation processes occurring in plutonic settings are more complex (e.g. Janoušek and Moyen, 2020), this straightforward approach can accurately reproduce the Fe isotopic trends in the BPZP.

8. Implications

I-type granitoids like the BPZP are the most abundant granite type in the upper continental crust (e.g. Kemp et al., 2007). In the BPZP, whole rock $\delta^{56}Fe$ is controlled by the balance between crystallisation of isotopically light silicates (biotite and hornblende) and isotopically heavy magnetite. Crystallisation drives a muted increase in $\delta^{56}Fe$ with differentiation, as demonstrated mathematically using the Rayleigh equation. Hence, this is the extent of Fe isotopic fractionation to be expected in a simple calc-alkaline system undergoing fractional crystallisation in the absence of additional processes (i.e. crustal contamination, fluid alteration, addition of new batches of magma). The restricted range in whole rock $\delta^{56}Fe$ observed and modelled in the BPZP matches the observation that I-type granitic rocks globally have low $\delta^{56}Fe$ values <0.2‰ (Foden et al., 2015).

Although the BPZP is interpreted to form by progressive fractional crystallisation of a liquid body of magma, it is likely that such liquid-dominant bodies of magma are rare in the crust. Instead, magma reservoirs are recognised to be “mushy” regions composed of non-eruptible crystal frameworks and interstitial melt (Bachmann and Bergantz, 2004; Hildreth, 2004). There remain questions surrounding the exact crystal-melt segregation and differentiation processes (e.g. Bachmann and Bergantz, 2004; Holness, 2018) and temperature regimes (e.g. Barboni et al., 2016; Rubin et al., 2017) in these mushes. However, if we consider that the larger, more complex mush bodies are formed of smaller plutonic units where magmatic processes are similar to the BPZP, this study provides a necessary baseline understanding of the behaviour of Fe isotopes to enable future investigation of more complex mushes.

A key finding from this study is that the $\Delta^{56}Fe_{mag\text{-}bt}$ values measured in the BPZP at temperatures >690 °C show close agreement with temperature dependent expressions derived from NRIXS and *ab initio* data (Figure 9). Additionally, the $\Delta^{56}Fe_{mag\text{-}bt}$ values measured in the BPZP match temperature dependent expressions derived from mineral separates in a banded iron formation metamorphosed

at 538°C (Ye et al., 2020; Figure 9). Hence, the BPZP study demonstrates the validity of these expressions when extended to higher temperatures. Mineral separates from a metamorphosed ironstone and an I-type granite will have experienced different P-T-X-fO_2 conditions during crystallisation. Therefore, the agreement between $\Delta^{56}Fe_{mag\text{-}bt}$ values from two vastly different geological settings suggests that inter-mineral fractionation factors between the same mineral pair in different samples is overwhelmingly controlled by temperature, rather than variations in chemical composition and/or fO_2.

The similarity between inter-mineral fractionation factors from a range of geological settings, temperatures, compositions and fO_2 conditions demonstrates the wide applicability of Fe isotopes to addressing problems in igneous geology. Specifically, in crystal mushes, inter-mineral fractionation factors between phases at equilibrium could be used to provide information about magma storage temperatures. This is especially useful in plutonic settings because of the lack of appropriate geothermometers when coexisting liquid composition cannot be easily determined (e.g. Putirka, 2016). If crystallisation temperature is known, inter-mineral fractionation factors can also be used to test for isotopic equilibrium between phases. Although the BPZP mineral separates obtain Fe isotopic equilibrium during fractional crystallisation, differentiation processes in larger mush bodies are thought to be more complex. Mush regions are often open systems, and if processes such as magma recharge, mixing, reactive porous flow and crustal assimilation occur, crystal scale isotopic disequilibrium may be expected. Therefore, the application of stable isotopic compositions to the investigation of more complex mushy systems to determine features like the range of storage temperatures and the extent of isotopic (dis)equilibrium during differentiation is a promising avenue of future research.

As Fe is present in multiple redox states, previous studies have investigated the potential link between Fe isotopic composition of mineral separates and/or whole rock powders and magma fO_2 during magmatic differentiation (e.g. Williams et al., 2005; Sossi et al., 2012; Foden et al., 2015). Although magma fO_2 will control the fractionating mineral assemblage, leading to distinct trends in whole rock $\delta^{56}Fe$ for I-, A- and S-type granites (Foden et al., 2015), this study has demonstrated that variation in mineral $Fe^{3+}/\Sigma Fe$ does not have a resolvable effect on Fe isotope fractionation factors between specific mineral pairs, suggesting limited use of Fe isotopes in mineral phases as a direct fO_2 proxy. A problem with Fe is that it is present as a major element in all silicate and oxide phases, and Fe isotopes are fractionated by a multitude of processes. However, the isotopic composition of trace elements concentrated in only one mineral may have potential as fO_2 proxies. A possibility is vanadium isotopes, where experimental studies suggest relationship between magnetite-melt V fractionation factors and magma fO_2 (Sossi et al., 2018b). Therefore, combining a well-studied isotope system of a major element like Fe with isotopes of a trace element like V may provide further understanding about P-T-X-fO_2 conditions during magmatic differentiation.

9. Conclusion

The Boggy Plain Zoned Pluton is a useful natural system for investigating Fe isotope fractionation during closed system fractional crystallisation of an I-type magma. This is the first time that the Fe isotopic composition of mineral separates have been measured in a closed system I-type suite. This has permitted the derivation of new mineral-melt fractionation factors which are representative of the X-T-fO_2 conditions in calc-alkaline settings.

1. In the BPZP, whole rock $\delta^{56}Fe$ increases from 0.038‰ to 0.171‰ with decreasing MgO content. Whole rock $\delta^{66}Zn$ is not affected by fractional crystallisation, but fluid alteration may cause the heavy $\delta^{66}Zn$ signal observed in aplite samples. A lack of coupling between $\delta^{56}Fe$ and $\delta^{66}Zn$ strongly suggests that Fe isotopes are not fractionated by fluid exsolution, thus Fe isotopic variation is dominantly controlled by fractional crystallisation.
2. Minerals show heavy Fe isotope enrichment in the order magnetite > biotite = hornblende > orthopyroxene. Mineral separates display inter-mineral Fe isotopic equilibrium. Inter-mineral fractionation factors match previous empirical and theoretical estimates from a range of P-T-X-fO_2 conditions.
3. Mineral separate data can be used to derive temperature dependent fractionation factors for magnetite and hydrous silicates in calc-alkaline settings: $\Delta^{56}Fe_{mag\text{-}bt} = 0.28x10^6/T^2$, $\Delta^{56}Fe_{mag\text{-}melt} = 0.17x10^6/T^2$ and $\Delta^{56}Fe_{bt/hbd\text{-}melt} = -0.12x10^6/T^2$. These are used to construct internally consistent, temperature dependent models of Fe isotopic fractionation during fractional crystallisation of a calc-alkaline magma.
4. The strong temperature dependence on equilibrium Fe isotopic fractionation highlights future avenues of research for the use of Fe isotopes in investigating petrogenetic processes and physical conditions in crystal mush bodies.

Acknowledgements

This research was supported by a NERC IAPETUS Doctoral Training Programme (NE/L002590/1) studentship to MAS. Doone Wyborn and Hugh O'Neill are thanked for fieldwork assistance during JP's visit to ANU in 2013, funded by Australian Research Council Discovery Grant DP130101355 to H.St.C. O'Neill and JP. JP thanks Doone Wyborn and Bruce Chappell for many interesting discussions about granite petrogenesis during her 2013 visit. We appreciate the efficient editorial handling of M. Roskosz and thank Nicole Nie, Luc Doucet and one anonymous reviewer for constructive reviews which greatly improved the manuscript.

Appendix A: Supplementary Material

Supplementary Material 1: Petrographic descriptions, Neodymium isotopic analyses, Rhyolite MELTS modelling

Supplementary Material 2: Thin section scans in plane polarized light

Supplementary Material 3: Research Data

References

Archer C., Andersen M. B., Cloquet C., Conway T. M., Dong S., Ellwood M., Moore R., Nelson J., Rehkämper M., Rehkämper R., Rouxel O., Samanta M., Shin K.-C., Sohrin Y., Takano S. and Wasylenki L. (2017) Inter-calibration of a proposed new primary reference standard AA-ETH Zn for zinc isotopic analysis. *J. Anal. At. Spectrom.* **32**, 415–419.

Bachmann O. and Bergantz G. W. (2004) On the Origin of Crystal-poor Rhyolites: Extracted from Batholithic Crystal Mushes. *J. Petrol.* **45**, 1565–1582.

Bachmann O. and Huber C. (2019) The Inner Workings of Crustal Distillation Columns; the Physical Mechanisms and Rates Controlling Phase Separation in Silicic Magma Reservoirs. *J. Petrol.* **60**, 3–18.

Barboni M., Boehnke P., Schmitt A. K., Mark Harrison T., Shane P., Bouvier A. S. and Baumgartner L. (2016) Warm storage for arc magmas. *Proc. Natl. Acad. Sci.* **113**, 13959–13964.

Barnes C. G., Werts K., Memeti V. and Ardill K. (2019) Most Granitoid Rocks are Cumulates: Deductions from Hornblende Compositions and Zircon Saturation. *J. Petrol.* **60**, 2227–2240.

Blanchard, M., Poitrasson, F., Méheut, M., Lazzeri, M., Mauri, F. and Balan, E. (2009). Iron isotope fractionation between pyrite (FeS_2), hematite (Fe_2O_3) and siderite ($FeCO_3$): A first-principles density functional theory study. *Geochim. Cosmochim. Acta* **73**, 6565-6578.

Burton-Johnson A., Macpherson C. G., Ottley C. J., Nowell G. M. and Boyce A. J. (2019) Generation of the Mt Kinabalu Granite by Crustal Contamination of Intraplate Magma Modelled by Equilibrated Major Element Assimilation with Fractional Crystallization (EME-AFC). *J. Petrol.* **60**, 1461–1487.

Cao Y., Wang C. Y., Huang F. and Zhang Z. (2019) Iron Isotope Systematics of the Panzhihua Mafic Layered Intrusion Associated With Giant Fe-Ti Oxide Deposit in the Emeishan Large Igneous Province, SW China. *J. Geophys. Res. Solid Earth* **124**, 358–375.

Cashman K. V, Sparks R. S. J. and Blundy J. D. (2017) Vertically extensive and unstable magmatic systems: A unified view of igneous processes. *Science* **355**.

Chappell B. W., Bryant C. J. and Wyborn D. (2012) Peraluminous I-type granites. *Lithos* **153**, 142–153.

Chappell, B. W., and White, A. J. (2001). Two contrasting granite types: 25 years later. *Aust. J. Earth Sci.* **48**, 489-499.

Chappell B. W. and Wyborn D. (2004) Cumulate and Cumulative Granites and Associated Rocks. *Resour. Geol.* **54**, 227–240.

Chen H., Savage P. S., Teng F. Z., Helz R. T. and Moynier F. (2013) Zinc isotope fractionation during magmatic differentiation and the isotopic composition of the bulk Earth. *Earth Planet. Sci. Lett.* **369**, 34–42.

Chen L.-M., Song X.-Y., Zhu X.-K., Zhang X.-Q., Yu S.-Y. and Yi J.-N. (2014) Iron isotope fractionation during crystallization and sub-solidus re-equilibration: Constraints from the Baima mafic layered intrusion, SW China. *Chem. Geol.* **380**, 97–109.

Chen S., Liu Y., Hu J., Zhang Z., Hou Z. and Yu H. (2015) Zinc Isotopic Compositions of NIST SRM 683 and Whole-Rock Reference Materials. *Geostand. Geoanalytical Res.* **40**, 417-432.

Craddock P. R. and Dauphas N. (2011) Iron Isotopic Compositions of Geological Reference Materials and Chondrites. *Geostand. Geoanalytical Res.* **35**, 101–123.

Czamanske G. K. and Wones D. R. (1973) Oxidation During Magmatic Differentiation, Finnmarka Complex, Oslo Area, Norway: Part 2, The Mafic Silicates. *J. Petrol.* **14**, 349–380.

Dauphas N., Roskosz M., Alp E. E., Golden D. C., Sio C. K., Tissot F. L. H., Hu M. Y., Zhao J., Gao L. and Morris R. V. (2012) A general moment NRIXS approach to the determination of equilibrium Fe isotopic fractionation factors: Application to goethite and jarosite. *Geochim. Cosmochim. Acta* **94**, 254–275.

Dauphas N., Roskosz M., Alp E. E., Neuville D. R., Hu M. Y., Sio C. K., Tissot F. L. H., Zhao J., Tissandier L., Médard E. and Cordier C. (2014) Magma redox and structural controls on iron isotope variations in Earth's mantle and crust. *Earth Planet. Sci. Lett.* **398**, 127–140.

Dauphas N., John S. G. and Rouxel O. (2017) Iron Isotope Systematics. *Rev. Mineral. Geochemistry* **82**, 415–510.

Doucet L. S., Laurent O., Mattielli N. and Debouge W. (2018) Zn isotope heterogeneity in the continental lithosphere: New evidence from Archean granitoids of the northern Kaapvaal craton, South Africa. *Chem. Geol.* **476**, 260–271.

Doucet, L. S., Laurent, O., Ionov, D. A., Mattielli, N., Debaille, V. and Debouge, W. (2020) Archean lithospheric differentiation: Insights from Fe and Zn isotopes. *Geology* **48**, 1028-1032.

Du D. H., Li W., Wang X. L., Shu X. J., Yang T. and Sun T. (2019) Fe isotopic fractionation during the magmatic–hydrothermal stage of granitic magmatism. *Lithos* **350–351**.

Du D.-H., Wang X.-L., Yang T., Chen X., Li J.-Y. and Li W. (2017) Origin of heavy Fe isotope compositions in high-silica igneous rocks: A rhyolite perspective. *Geochim. Cosmochim. Acta* **218**, 58–72.

Dziony W., Horn I., Lattard D., Koepke J., Steinhoefel G., Schuessler J. A. and Holtz F. (2014) In-situ Fe isotope ratio determination in Fe–Ti oxides and sulfides from drilled gabbros and basalt from the IODP Hole 1256D in the eastern equatorial Pacific. *Chem. Geol.* **363**, 101–113.

Foden J., Sossi P. A. and Wawryk C. M. (2015) Fe isotopes and the contrasting petrogenesis of A-, I- and S-type granite. *Lithos* **212–215**, 32–44.

Frost B. R. and Lindsley D. H. (1991) Oxide Minerals: petrologic and magnetic significance. In *Reviews in Mineralogy and Geochemistry* (ed. D. H. Lindsley). pp. 433–468.

Fujii T., Moynier F., Blichert-Toft J. and Albarède F. (2014) Density functional theory estimation of isotope fractionation of Fe, Ni, Cu, and Zn among species relevant to geochemical and biological environments. *Geochim. Cosmochim. Acta* **140**, 553–576.

Gajos N. A., Lundstrom C. C. and Taylor A. H. (2016) Spatially controlled Fe and Si isotope variations: an alternative view on the formation of the Torres del Paine pluton. *Contrib. to Mineral. Petrol.* **171**, 93.

Ghiorso M. S. and Gualda G. A. R. (2015) An H2O–CO2 mixed fluid saturation model compatible with rhyolite-MELTS. *Contrib. to Mineral. Petrol.* **169**, 53.

Gleeson M. L. M., Gibson S. A. and Williams H. M. (2020) Novel insights from Fe-isotopes into the lithological heterogeneity of Ocean Island Basalts and plume-influenced MORBs. *Earth Planet. Sci. Lett.* **535**.

Gualda G. A. R., Ghiorso M. S., Lemons R. V. and Carley T. L. (2012) Rhyolite-MELTS: a Modified Calibration of MELTS Optimized for Silica-rich, Fluid-bearing Magmatic Systems. *J. Petrol.* **53**, 875–890.

He Y., Wu H., Ke S., Liu S. A. and Wang Q. (2017) Iron isotopic compositions of adakitic and non-adakitic granitic magmas: Magma compositional control and subtle residual garnet effect. *Geochim. Cosmochim. Acta* **203**, 89–102.

Heimann A., Beard B. L. and Johnson C. M. (2008) The role of volatile exsolution and sub-solidus fluid/rock interactions in producing high 56Fe/54Fe ratios in siliceous igneous rocks. *Geochim. Cosmochim. Acta* **72**, 4379–4396.

Hiebert R. S., Bekker A., Houlé M. G., Wing B. A. and Rouxel O. J. (2016) Tracing sources of crustal contamination using multiple S and Fe isotopes in the Hart komatiite-associated Ni–Cu–PGE sulfide deposit, Abitibi greenstone belt, Ontario, Canada. *Miner. Depos.* **51**, 919–935.

Hildreth W. (2004) Volcanological perspectives on Long Valley, Mammoth Mountain, and Mono Craters: Several contiguous but discrete systems. *J. Volcanol. Geotherm. Res.* **136**, 169–198.

Holland T. and Blundy J. (1994) Non-ideal interactions in calcic amphiboles and their bearing on amphibole-plagioclase thermometry. *Contrib. to Mineral. Petrol.* **116**, 433–447.

Holness M. B. (2018) Melt segregation from silicic crystal mushes: a critical appraisal of possible mechanisms and their microstructural record. *Contrib. to Mineral. Petrol.* **173**, 48.

Hoskin P. W. O., Kinny P. D., Wyborn D. and Chappell B. W. (2000) Identifying accessory mineral saturation during differentiation in granitoid magmas: An integrated approach. *J. Petrol.* **41**, 1365–1396.

Huang J., Zhang X. C., Chen S., Tang L., Wörner G., Yu H. and Huang F. (2018) Zinc isotopic systematics of Kamchatka-Aleutian arc magmas controlled by mantle melting. *Geochim. Cosmochim. Acta* **238**, 85–101.

Ickert R. B. (2010) U-Pb, Lu-Hf, and O isotope systematics of zircon from southeastern Australian Siluro-Devonian granites. Ph. D. thesis, Australian National University

Ickert R. B., Williams I. S. and Wyborn D. (2011) Ti in zircon from the Boggy Plain zoned pluton: implications for zircon petrology and Hadean tectonics. *Contrib. to Mineral. Petrol.* **162**, 447–461.

Iles K. A. (2017) Isotopic disequilibrium in granitic systems: the origins of heterogeneity in granites and implications for partial melting in the crust and petrogenetic models. Ph. D. thesis, University of Melbourne

Irvine T. N. (1982) Terminology for Layered Intrusions. *J. Petrol.* **23**, 127–162.

Jackson M. D., Blundy J. and Sparks R. S. J. (2018) Chemical differentiation, cold storage and remobilization of magma in the Earth's crust. *Nature* **564**, 405–409.

Janoušek V. and Moyen J.-F. (2020) Whole-rock geochemical modelling of granite genesis: the current state of play. *Geol. Soc. London, Spec. Publ.* **491**, 267–291.

Kemp A. I. S., Hawkesworth C. J., Foster G. L., Paterson B. A., Woodhead J. D., Hergt J. M., Gray C. M. and Whitehouse M. J. (2007) Magmatic and crustal differentiation history of granitic rocks from Hf-O isotopes in zircon. *Science* **315**, 980–983.

Leake B. E., Woolley A. R., Arps C. E. S., Birch W. D., Grice J. D., Hawthorne F. C., Kato A., Kisch H. J., Krivovichev V. G., Linthout K., Laird J., Mandarino J. A., Maresch W. V., Nickel E. H., Rock N. M. S., Schumacher J. C., Smith D. C., Stephenson N. C. N., Ungaretti L., Whittaker E. J. and Youzhi, G. (1997) Nomenclature of amphiboles: report of the subcommittee on amphiboles of the International Mineralogical Association, commission on new minerals and mineral names. *Can. Mineral.* **35**, 219–246.

Liu S. A., Li D., Li S., Teng F. Z., Ke S., He Y. and Lu Y. (2014) High-precision copper and iron isotope analysis of igneous rock standards by MC-ICP-MS. *J. Anal. At. Spectrom.* **29**, 122–133.

Ludington S. (1978) The biotite-apatite geothermometer revisited. *Am. Mineral.* **63**, 551–553.

Maréchal C. N., Télouk P. and Albarède F. (1999) Precise analysis of copper and zinc isotopic compositions by plasma-source mass spectrometry. *Chem. Geol.* **156**, 251–273.

McCoy-West A. J., Fitton J. G., Pons M.-L., Inglis E. C. and Williams H. M. (2018) The Fe and Zn isotope composition of deep mantle source regions: Insights from Baffin Island picrites. *Geochim. Cosmochim. Acta* **238**, 542–562.

Moynier F., Vance D., Fujii T. and Savage P. (2017) The Isotope Geochemistry of Zinc and Copper. *Rev. Mineral. Geochemistry* **82**, 543–600.

Nebel O., Sossi P. A., Ivanic T. J., Bénard A., Gardiner N. J., Langford R. L. and Arculus R. J. (2020) Incremental Growth of Layered Mafic-Ultramafic Intrusions Through Melt Replenishment into a Crystal Mush Zone Traced by Fe-Hf Isotope Systematics. *Front. Earth Sci.* **8**, 2.

Nie N. X., Dauphas N., Alp E. E., Zeng H., Sio C. K., Hu J. Y., Chen X., Aarons S. M., Zhang Z., Tian H.-C., Wang D., Prissel K. B., Greer J., Bi W., Hu M. Y., Zhao J., Shahar A., Roskosz M., Teng F.-Z., Krawczynski M. J., Heck P. R. and Spear F. S. (2021) Iron, magnesium, and titanium isotopic fractionations between garnet, ilmenite, fayalite, biotite, and tourmaline: Results from NRIXS, ab initio, and study of mineral separates from the Moosilauke metapelite. *Geochim. Cosmochim. Acta* **302**, 18–45.

Park J. W., Campbell I. H., Ickert R. B. and Allen C. M. (2013) Chalcophile element geochemistry of the Boggy Plain zoned pluton, southeastern Australia: A S-saturated barren compositionally diverse magmatic system. *Contrib. to Mineral. Petrol.* **165**, 217–236.

Poitrasson F. and Freydier R. (2005) Heavy iron isotope composition of granites determined by high resolution MC-ICP-MS. *Chem. Geol.* **222**, 132–147.

Polyakov V. B., Clayton R. N., Horita J. and Mineev S. D. (2007) Equilibrium iron isotope fractionation factors of minerals: Reevaluation from the data of nuclear inelastic resonant X-ray scattering and Mössbauer spectroscopy. *Geochim. Cosmochim. Acta* **71**, 3833–3846.

Polyakov V. B. and Mineev S. D. (2000) The use of Mossbauer spectroscopy in stable isotope geochemistry. *Geochim. Cosmochim. Acta* **64**, 849–865.

Putirka K. (2016) Amphibole thermometers and barometers for igneous systems and some implications for eruption mechanisms of felsic magmas at arc volcanoes. *Am. Mineral.* **101**, 841–858.

Putirka K. D. (2008) Thermometers and barometers for volcanic systems. *Rev. Mineral. Geochemistry* **69**, 61–120.

Rabin S., Blanchard M., Pinilla C., Poitrasson F. and Gregoire M. (2021) First-principles calculation of iron and silicon isotope fractionation between Fe-bearing minerals at magmatic temperatures: The importance of second atomic neighbors. *Geochim. Cosmochim. Acta*. **304**, 101-118.

Rieder M., Cavazzini G., D'Yakonov, Y. S. D., Frank-Kamenetskii V. A., Gottardi G., Guggenheim S., Koval P. V., Müller G., Neiva A. M. R., Radoslovich E. W., Robert J., Sassi F. P., Takeda H., Weiss Z. and Wones D. R. (1999) Nomenclature of the micas. *Mineral. Mag.* **63**, 267–279.

Roskosz M., Sio C. K. I., Dauphas N., Bi W., Tissot F. L. H., Hu M. Y., Zhao J. and Alp E. E. (2015) Spinel-olivine-pyroxene equilibrium iron isotopic fractionation and applications to natural peridotites. *Geochim. Cosmochim. Acta* **169**, 184–199.

Rubin A. E., Cooper K. M., Till C. B., Kent A. J. R., Costa F., Bose M., Gravley D., Deering C. and Cole J. (2017) Rapid cooling and cold storage in a silicic magma reservoir recorded in individual crystals. *Science* **356**, 1154–1157.

Schauble E. A. (2004) Applying stable isotope fractionation theory to new systems. *Rev. Mineral. Geochemistry* **55**, 65–111.

Schoenberg R. and von Blanckenburg F. (2006) Modes of planetary-scale Fe isotope fractionation. *Earth Planet. Sci. Lett.* **252**, 342–359.

Schoenberg, R., Marks, M. A. W., Schuessler, J. A., von Blanckenburg, F. and Markl, G. (2009) Fe isotope systematics of coexisting amphibole and pyroxene in the alkaline igneous rock suite of the Ilímaussaq Complex, South Greenland. *Chem. Geol.* **258**, 65-77.

Schuessler J. A., Schoenberg R. and Sigmarsson O. (2009) Iron and lithium isotope systematics of the Hekla volcano, Iceland — Evidence for Fe isotope fractionation during magma differentiation. *Chem. Geol.* **258**, 78–91.

Shahar A., Young E. D. and Manning C. E. (2008) Equilibrium high-temperature Fe isotope fractionation between fayalite and magnetite: An experimental calibration. *Earth Planet. Sci. Lett.* **268**, 330–338.

Shannon R. D. (1976) Revised Effective Ionic Radii and Systematic Studies of Interatomic Distances in Halides and Chalcogenides. *Acta Crystallogr. Sect. A* **32**, 751–767.

Sisson T. W. and Grove T. L. (1993) Mineralogy and Petrology Experimental investigations of the role of H20 in calc-alkaline differentiation and subduction zone magmatism. *Contrib. to Mineral. Petrol.* **113**, 143–166.

Soderman C. R., Matthews S., Shorttle O., Jackson M. G., Ruttor S., Nebel O., Turner S., Beier C., Millet M. A., Widom E., Humayun M. and Williams H. M. (2021) Heavy δ57Fe in ocean island basalts: A non-unique signature of processes and source lithologies in the mantle. *Geochim. Cosmochim. Acta* **292**, 309–332.

Sossi P. A., Foden J. D. and Halverson G. P. (2012) Redox-controlled iron isotope fractionation during magmatic differentiation: an example from the Red Hill intrusion, S. Tasmania. *Contrib. to Mineral. Petrol.* **164**, 757–772.

Sossi P. A., Nebel O. and Foden J. (2016) Iron isotope systematics in planetary reservoirs. *Earth Planet. Sci. Lett.* **452**, 295–308.

Sossi P. A., Halverson G. P., Nebel O. and Eggins S. M. (2015) Combined separation of Cu, Fe and Zn from rock matrices and improved analytical protocols for stable isotope determination. *Geostand. Geoanalytical Res.* **39**, 129–149.

Sossi P. A. and O'Neill H. S. C. (2017) The effect of bonding environment on iron isotope fractionation between minerals at high temperature. *Geochim. Cosmochim. Acta* **196**, 121–143.

Sossi P. A., Nebel O., O'Neill H. S. C. and Moynier F. (2018a) Zinc isotope composition of the Earth and its behaviour during planetary accretion. *Chem. Geol.* **477**, 73–84.

Sossi P. A., Prytulak J. and O'Neill H. S. C. (2018b) Experimental calibration of vanadium partitioning and stable isotope fractionation between hydrous granitic melt and magnetite at 800 °C and 0.5 GPa. *Contrib. to Mineral. Petrol.* **173**.

Sparks R. S. J., Annen C., Blundy J. D., Cashman K. V., Rust A. C. and Jackson M. D. (2019) Formation and dynamics of magma reservoirs. *Philos. Trans. R. Soc. A.* **377**.

Telus M., Dauphas N., Moynier F., Tissot F. L., Teng F.-Z., Nabelek P. I., Craddock P. R. and Groat L. A. (2012) Iron, zinc, magnesium and uranium isotopic fractionation during continental crust

differentiation: The tale from migmatites, granitoids, and pegmatites. *Geochim. Cosmochim. Acta* **97**, 247–265.

Teng F.-Z., Dauphas N. and Helz R. T. (2008) Iron Isotope Fractionation During Magmatic Differentiation in Kilauea Iki Lava Lake. *Science* **320**, 1620–1622.

Tindle A. G. and Pearce J. A. (1981) Petrogenetic Modelling of in situ Fractional Crystallization in the Zoned Loch Doon Pluton, Scotland. *Contrib. to Mineral. Petrol.* **78**, 196–207.

Urey H. C. (1947) The Thermodynamic Properties of Isotopic Substances. *J. Chem. Soc.*, 562–581.

Vernon R. H. and Collins W. J. (2011) Structural Criteria for Identifying Granitic Cumulates. *J. Geol.* **119**, 127–142.

Wang Z.-Z., Liu S.-A., Liu J., Huang J., Xiao Y., Chu Z.-Y., Zhao X.-M. and Tang L. (2017) Zinc isotope fractionation during mantle melting and constraints on the Zn isotope composition of Earth's upper mantle. *Geochim. Cosmochim. Acta* **198**, 151–167.

Wang Z.-Z., Liu S.-A., Liu Z.-C., Zheng Y.-C. and Wu F.-Y. (2020) Extreme Mg and Zn isotope fractionation recorded in the Himalayan leucogranites. *Geochim. Cosmochim. Acta* **278**, 305–321.

Weinberg R. F., Vernon R. H. and Schmeling, H. (2021) Processes in mushes and their role in the differentiation of granitic rocks. *Earth-Science Reviews*, **220**.

Wells P. R. A. (1977) Pyroxene Thermometry in Simple and Complex Systems. *Contrib. to Mineral. Petrol.* **62**, 129–139.

Weyer S. and Ionov D. A. (2007) Partial melting and melt percolation in the mantle: The message from Fe isotopes. *Earth Planet. Sci. Lett.* **259**, 119–133.

Williams H. M., Peslier A. H., McCammon C., Halliday A. N., Levasseur S., Teutsch N. and Burg J.-P. (2005) Systematic iron isotope variations in mantle rocks and minerals: The effects of partial melting and oxygen fugacity. *Earth Planet. Sci. Lett.* **235**, 435–452.

Williams H. M., Prytulak J., Woodhead J. D., Kelley K. A., Brounce M. and Plank T. (2018) Interplay of crystal fractionation, sulfide saturation and oxygen fugacity on the iron isotope composition of arc lavas: An example from the Marianas. *Geochim. Cosmochim. Acta* **226**, 224–243.

Williams H. M. and Bizimis M. (2014) Iron isotope tracing of mantle heterogeneity within the source regions of oceanic basalts. *Earth Planet. Sci. Lett.* **404**, 396–407.

Wu H., He Y., Bao L., Zhu C. and Li S. (2017) Mineral composition control on inter-mineral iron isotopic fractionation in granitoids. *Geochim. Cosmochim. Acta* **198**, 208–217.

Wyborn D., Chappell B. W. and James M. (2001) Examples of convective fractionation in high-temperature granites from the Lachlan Fold Belt. *Aust. J. Earth Sci.* **48**, 531–541.

Wyborn D., Turner B. S. and Chappell B. W. (1987) The Boggy Plain Supersuite: A distinctive belt of I-type igneous rocks of potential economic significance in the Lachlan Fold Belt. *Aust. J. Earth Sci.* **34**, 21–43.

Wyborn D. (1983) Fractionation Processes in the Boggy Plain Zoned Pluton. Ph. D. thesis, Australian National University

Xia Y., Li S. and Huang F. (2017) Iron and Zinc isotope fractionation during magmatism in the continental crust: Evidence from bimodal volcanic rocks from Hailar basin, NE China. *Geochim. Cosmochim. Acta* **213**, 35–46.

Xu L. J., He Y., Wang S. J., Wu H. and Li S. (2017) Iron isotope fractionation during crustal anatexis: Constraints from migmatites from the Dabie orogen, Central China. *Lithos* **284**, 171–179.

Xu L. J., Liu S. A., Wang Z. Z., Liu C. and Li S. (2019) Zinc isotopic compositions of migmatites and granitoids from the Dabie Orogen, central China: Implications for zinc isotopic fractionation during differentiation of the continental crust. *Lithos* **324–325**, 454–465.

Ye H., Wu C., Brzozowski M. J., Yang T., Zha X., Zhao S., Gao B. and Li W. (2020) Calibrating equilibrium Fe isotope fractionation factors between magnetite, garnet, amphibole, and biotite. *Geochim. Cosmochim. Acta* **271**, 78–95.

Young E. D., Galy A. and Nagahara H. (2002) Kinetic and equilibrium mass-dependent isotope fractionation laws in nature and their geochemical and cosmochemical significance. *Geochim. Cosmochim. Acta* **66**, 1095–1104.

Zajacz Z., Halter W. E., Pettke T. and Guillong M. (2008) Determination of fluid/melt partition coefficients by LA-ICPMS analysis of co-existing fluid and silicate melt inclusions: Controls on element partitioning. *Geochim. Cosmochim. Acta* **72**, 2169–2197.

Zambardi T., Lundstrom C. C., Li X. and McCurry M. (2014) Fe and Si isotope variations at Cedar Butte volcano; insight into magmatic differentiation. *Earth Planet. Sci. Lett.* **405**, 169–179.

Zimmer M. M., Plank T., Hauri E. H., Yogodzinski G. M., Stelling P., Larsen J., Singer B., Jicha B., Mandeville C. and Nye C. J. (2010) The role of water in generating the calc-alkaline trend: New volatile data for aleutian magmas and a new tholeiitic index. *J. Petrol.* **51**, 2411–2444.

Table 1. Iron and Zinc isotopic composition of BPZP whole rock samples and USGS reference materials. Whole rock (WR) MgO content from Wyborn (1983). Iron isotopic ratios are quoted relative to the IRMM 014 standard. Zinc isotopic ratios were measured relative to the AA-ETH standard. These are recast relative to the JMC-Lyon standard using the correction of +0.280‰ (Archer et al., 2017). Errors are quoted as 2 standard deviations of the mean of all measurements of the sample. If <3 analyses could be made, errors are reported as 2SE (+).

Sample	**Rock Type**	**WR MgO (wt. %)**	**$\delta^{56}Fe_{IRMM-014}$ (‰)**	**2SD**	**$\delta^{57}Fe_{IRMM-014}$ (‰)**	**2SD**	**n**	**$\delta^{66}Zn_{JMC-Lyon}$ (‰)**	**$\delta^{66}Zn_{AA-ETH}$ (‰)**	**2SD**	**$\delta^{68}Zn_{AA-ETH}$ (‰)**	**2SD**	**n**
BP34	Diorite	8.32	0.038	0.024	0.062	0.044	3	0.222	-0.058	0.017	-0.106	0.013	3
BP1	Diorite	7.58	0.045	0.018	0.059	0.031	3	0.226	-0.054	0.042	-0.115	0.104	3
BP39	Diorite	6.78	0.078	0.044	0.136	0.072	3	0.275	-0.005	0.041	0.011	0.056	3
BP40	Granodiorite	5.32	0.074	0.034	0.108	0.046	4	0.282	0.002	0.031	0.057	0.041	3
BP26	Granodiorite	4.48	0.092	0.043	0.129	0.066	5	0.288	0.008	0.021	0.074	0.084	3
BP23	Granodiorite	3.56	0.082	0.040	0.113	0.047	3	0.305	0.025	0.008	0.081	0.034	3
BP29	Granite	3.34	0.092	0.011	0.130	0.009	3	0.353	0.073	0.014	0.180	0.029	3
BP22	Granite	2.69	0.175	0.009	0.290	0.047	6	0.254	-0.026	0.060	-0.063	0.093	4
BP28	Granite	2.40	0.104	0.045	0.154	0.024	4	0.296	0.016	0.021	0.048	0.018	3
BP11	Granite	0.96	0.162	0.029	0.234	0.030	4						
BP12	Aplite	0.52	0.171	0.032	0.253	0.013	3	0.603	0.323	0.009	0.665	0.041	3
BP42	Aplite	0.38	0.144	0.037	0.239	0.087	4	0.518	0.238	0.022+	0.477	0.025+	2
	Replicate		0.117	0.012	0.188	0.004	3						
USGS reference Materials													
GSP-2			0.150	0.033	0.217	0.034	13	0.956	0.676	0.059	0.954	0.104	3
BHVO-2			0.139	0.031	0.221	0.042	8						
BIR-1a			0.034	0.016	0.048	0.024	4	0.288	0.008	0.040	0.052	0.104	6

Table 2. Iron and Zinc isotopic composition of BPZP mineral separates. For mineral textures, I denotes interstitial phases, and P primocrysts. Iron isotopic ratios are quoted relative to the IRMM 014 standard. Zinc isotopic ratios were measured relative to the AA-ETH standard. These are recast relative to the JMC-Lyon standard using the correction of +0.280‰ (Archer et al., 2017). Errors are quoted as 2 standard deviations of the mean of all measurements of the sample.

Sample	**Mineral Phase**	**Texture**	**$\delta^{56}Fe_{IR}$ MM-014 (‰)**	**2SD**	**$\delta^{57}Fe$ IRMM-014 (‰)**	**2SD**	**n**	**$\delta^{66}Zn_{JM}$ C-Lyon (‰)**	**$\delta^{66}Zn$ AA-ETH (‰)**	**2SD**	**$\delta^{68}Zn$ AA-ETH (‰)**	**2SD**	**n**
BP41	Biotite	I	0.124	0.024	0.196	0.045	3	0.310	0.030	0.032	0.078	0.010	3
BP39	Orthopyroxene	P	-0.049	0.011	-0.063	0.054	4	0.235	-0.045	0.022	-0.133	0.025	3
	Biotite	I	0.095	0.034	0.146	0.065	8	0.257	-0.023	0.025	-0.091	0.025	3
	Hornblende	I	0.102	0.025	0.158	0.045	3	0.256	-0.024	0.035	0.033	0.019	3
	Magnetite	I	0.304	0.061	0.457	0.083	3	0.323	0.043	0.017	0.121	0.039	3
BP22	Biotite	P	-0.008	0.033	-0.004	0.062	7	0.235	-0.045	0.029	-0.132	0.018	3
	Hornblende	P	-0.005	0.030	0.009	0.056	3	0.268	-0.012	0.014	-0.079	0.029	3
	Magnetite	P	0.260	0.044	0.379	0.064	5	0.329	0.049	0.041	0.141	0.034	3
BP11	Biotite	P	0.030	0.020	0.048	0.038	3	0.271	-0.009	0.019	-0.049	0.015	3
	Hornblende	P	-0.007	0.011	-0.021	0.073	4	0.212	-0.068	0.039	-0.179	0.066	3
	Magnetite	P	0.320	0.050	0.481	0.081	4	0.198	-0.082	0.017	-0.187	0.039	3
BP42	Biotite	P	-0.009	0.012	0.014	0.048	4	0.530	0.250	0.032	0.461	0.097	3
	Magnetite	P	0.306	0.042	0.457	0.083	4	0.284	0.004	0.038	0.026	0.051	3

Table 3. Temperature determinations for the BPZP. Calculations from [1]Putirka (2008, Eq. 27b at 1.5kbar); [2]Holland and Blundy (1994, Edenite-richerite thermometer at 1.5kbar); [3]Ludington (1978); [4]Wells (1977). Values using [3] and [4] are given in Wyborn (1983). All mineral chemistry is from Wyborn (1983) and given in the Supplementary Information. [+]A crystallisation temperature was then chosen by only considering estimates where phases were present as primocrysts. *Uncertainty estimates for the thermometers are given as quoted in the literature. Given the typical uncertainties for each thermometer, each chosen temperature has an uncertainty estimate of approximately ±50°C. Mineral abbreviations as in Figure 3.

Sample	Primocryst Mineralogy	Temperature Estimates (°C)				Chosen Temperature (°C)[+]
		Two-Feldspar[1]	Hornblende-Plagioclase[2]	Biotite-Apatite[3]	Two-Pyroxene[4]	
BP39	opx, cpx, plag		751		865	865
BP22	plag, cpx, bt, hbd	806	724			724
BP11	plag, bt, hbd, kfs, qtz	769	648	674		697
BP42	Plag, bt, qtz, kfs			695		695
Uncertainty (°C)*		± 30	± 35-40	n/a	± 70	

Figure 1. (A) Map of the Berridale and Kosciuszko batholiths in the SE of the Lachlan Fold Belt (adapted from Ickert, 2010). The Boggy Plain Zoned Pluton is located in the North of the batholith. The sedimentary country rock is mostly Silurian-Ordovician aged turbidites and shales (Wyborn, 1983). (B) Geological map of the Boggy Plain Zoned pluton showing the concentric zonation from a gabbroic rim to a granitic core (adapted from Wyborn, 1983). The geological map is a reconstruction after subtracting 4.9km left lateral strike slip motion on the Boggy Plain Fault (Wyborn et al., 1987). The black dashed line shows the boundary between the inner and outer granodiorite. Sample localities are indicated by crosses; those in bold are ones from which mineral separates were picked.

Figure 2. Chemical variations in the BPZP. Whole rock compositional data from Wyborn (1983). Large symbols with bold outlines are those chosen for isotopic analysis in this study. The dashed line approximates the separation of liquids (<4.5 wt.% MgO) from cumulate rocks (>4.5 wt. % MgO; see text). The line also corresponds to the composition of sample BP26, which is used as the parental melt composition in subsequent models. The scatter in the granodiorite data (blue and purple squares) is attributed to the compositional zoning in the granodiorite.

Figure 3. Petrographic textures in the BPZP. (A) BP41 showing a typical cumulate texture, containing euhedral primocrysts of pyroxene and plagioclase, and minor interstitial biotite. (B) BP41 showing anhedral morphologies of interstitial biotite. (C) BP39 containing euhedral pyroxene primocrysts with biotite and hornblende rims. (D) BP40 transitional textures. Pyroxene cores surrounded by hornblende and biotite. (E) BP28 containing euhedral biotite and hornblende primocrysts, and no pyroxene present. (F) BP12 showing fine grained aplitic texture. Abbreviations opx = orthopyroxene, plag = plagioclase, ol= olivine, bt= biotite, hbd = hornblende, mag=titanomagnetite, kfs= K-feldspar. The BPZP samples are very coarse grained and therefore photomicrographs can show small scale features, but do not effectively demonstrate larger scale textural information. Full thin section scans are provided in the Supplementary Information.

Figure 4. Typical textures and morphologies of Fe-Ti oxides in the BPZP. (A) and (B) BP39 diorite, containing interstitial magnetite grains (white/yellow colour) with anhedral morphologies, showing granular exsolution of ilmenite and trellis exsolution of ilmenite (grey/brown colour). (C) and (D) BP22 granodiorites contain small, euhedral grains with very fine trellis exsolution lamellae. This is typical of magnetite grains in samples with WR MgO < 4.5 wt.%.

Figure 5. Three-isotope plots for (A) Fe (δ^{56}Fe vs δ^{57}Fe) and (B) Zn (δ^{66}Zn vs δ^{68}Zn). The slopes of the linear regressions are 1.47 and 2.01 respectively, which are consistent with the gradients predicted by mass dependent fractionation laws (i.e. ~1.5 and 2; Young et al., 2002).

Figure 6. Iron isotopic composition of whole rocks and mineral separates against WR MgO (A) and SiO_2 (B) content. Errors are plotted as 2SD of at least 3 individual measurements of each sample. A compilation of data from other plutonic I-type rocks is shown by the grey crosses (Poitrasson and Freydier, 2005; Schoenberg and von Blanckenburg, 2006; Heimann et al., 2008; Telus et al., 2012 and Foden et al., 2015). The vertical dashed line shows the divide between cumulate samples and liquids as in Figure 2. The blue shaded area is the estimate for the Bulk Silicate Earth from Sossi et al. (2016) of δ^{56}Fe = 0.033 ± 0.027‰.

Figure 7. Zinc isotopic compositions of whole rock and mineral separates against WR MgO (A) and SiO_2 (B) content. Errors are plotted as 2SD of at least 3 individual measurements of each sample. Grey crosses are co-genetic lavas from Hekla, Iceland (Chen et al., 2013). The vertical dashed line

shows the divide between cumulate samples and liquids as in Figure 2. Given that the pristine and depleted mantle have distinct Zn isotopic composition, and that heavy Zn isotopes can become concentrated in the melt during mantle partial melting (e.g. Wang et al., 2017; Huang et al., 2018; Sossi et al., 2018a), the average isotopic composition of mantle derived magmas from Chen et al., 2013 ($\delta^{66}Zn_{AA\text{-}ETH}$ of 0.01 ± 0.08‰) is shown by the blue shaded area for comparison.

Figure 8. Variation in magnetite-biotite fractionation factors with (A) WR SiO_2, (B) WR $Fe^{3+}/\Sigma Fe$ and (C) biotite $Fe^{3+}/\Sigma Fe$. Shaded symbols are when biotite and magnetite are both primocrysts. Open symbols are when biotite and magnetite are present as interstitial phases. Errors are the long term analytical uncertainty of ±0.05‰ (2SD) from measurement of solution standards.

Figure 9. Measured $\Delta^{56}Fe_{mag\text{-}bt}$ for the BPZP samples against crystallisation temperature (K). Filled circles are for primocryst biotite and hornblende. Open circles are interstitial biotite and hornblende. Errors in $\Delta^{56}Fe_{mag\text{-}bt}$ are given as ±0.05‰, the long-term analytical uncertainty for Fe. Errors in T as ±50K, as discussed in the Table 3 caption. The red triangle shows the measured $\Delta^{56}Fe_{mag\text{-}bt}$ from a metamorphosed ironstone in Ye et al. (2020) [1]. The red line and shaded area show the relationship $\Delta^{56}Fe_{mag\text{-}bt} = 0.28\ (\pm\ 0.07) \times 10^6/T^2$ from Ye et al. (2020) [1]. The blue line and shaded area show a theoretical estimate of $\Delta^{56}Fe_{mag\text{-}bt}$ calculated using NRIXS data, using Equation 1 after Dauphas et al. (2014). Values of 172 ± 16 N/m (Nie et al., 2021 [2]) and 264 ± 6 N/m (Roskosz et al., 2015 [3]) are used for the force constants of biotite and magnetite respectively, as discussed in the text. The green line and shaded area show a theoretical estimate of $\Delta^{56}Fe_{mag\text{-}bt}$ determined using values from *ab initio* calculations. Values of 207 N/m (Nie et al., 2021 [2]) and 292 N/m (Sossi and O'Neill, 2017 [4]) are used for the force constants of biotite and magnetite respectively, as discussed in the text. The error envelope considers a 5% error in the *ab initio* calculations.

Figure 10. Change in $\delta^{56}Fe$ of a magma undergoing fractional crystallisation (dashed lines), modelled using the Rayleigh equation ($\delta^{56}Fe = \delta^{56}Fe_i + (\Delta^{56}Fe_{min\text{-}melt} \times \ln f(Fe))$ at constant $\Delta^{56}Fe_{min\text{-}melt}$. BP26 was used as the starting magma composition. For the BPZP whole rock data (green triangles), f(Fe) is calculated based on changing MgO and FeO_{tot} content as described in the text. Previous studies have used the variation in concentration of incompatible elements (e.g. Rb, Th, U) to estimate F. However, concentrations of incompatible elements will also vary depending on the amount of trapped interstitial melt in the samples, so this method was not used. The blue shaded area is a weighted linear regression of the BPZP data from the start of the calculation until 2% Fe remains. This shows that the isotopic evolution for this part of the fractionation sequence can be described by a bulk $\Delta^{56}Fe_{min\text{-}melt}$ of approximately -0.03‰.

Figure 11. Determinations of modal abundances (A), bulk $\Delta^{56}Fe_{min\text{-}melt}$ (B), and resulting magma $\delta^{56}Fe$ (C) from three Rayleigh models. Green triangles show the isotopic composition of the BPZP WR samples. f(Fe) is calculated as described in the text. The blue error envelope shows magma $\delta^{56}Fe$ considering an error of ±0.03‰ on the fractionation factor expressions.

Figure 1

Click here to access/download;Figure;Fig1_New.eps

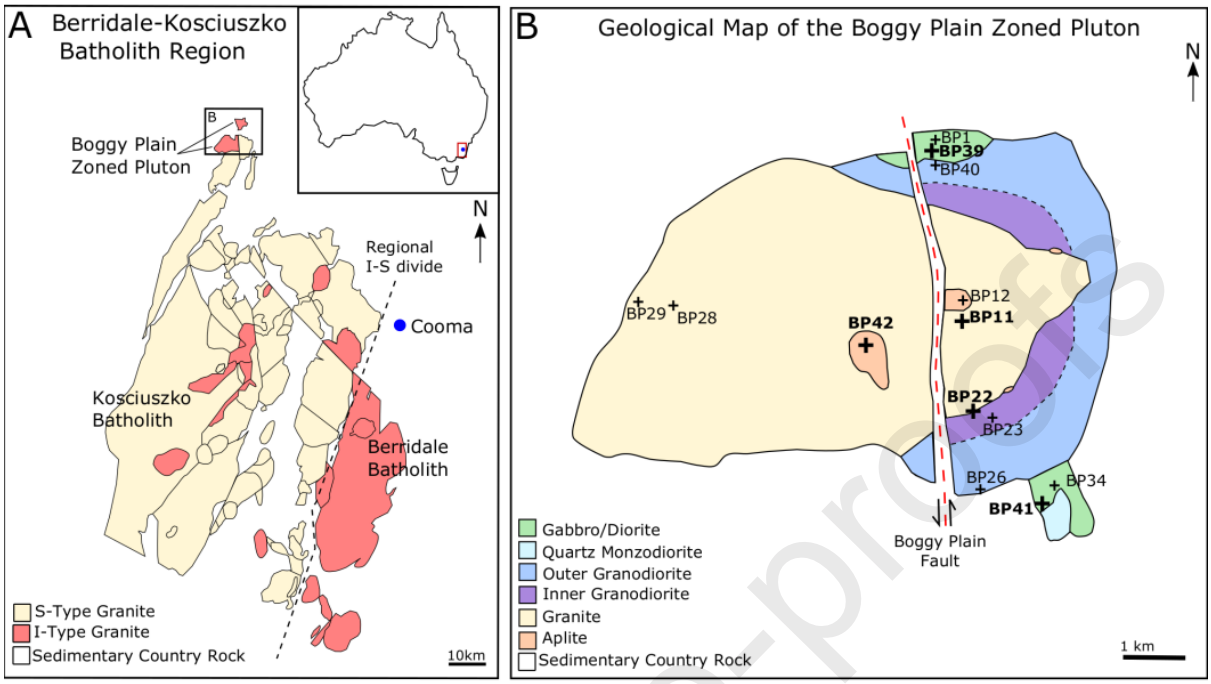

Figure 2

Click here to access/download;Figure;Fig2_New.eps

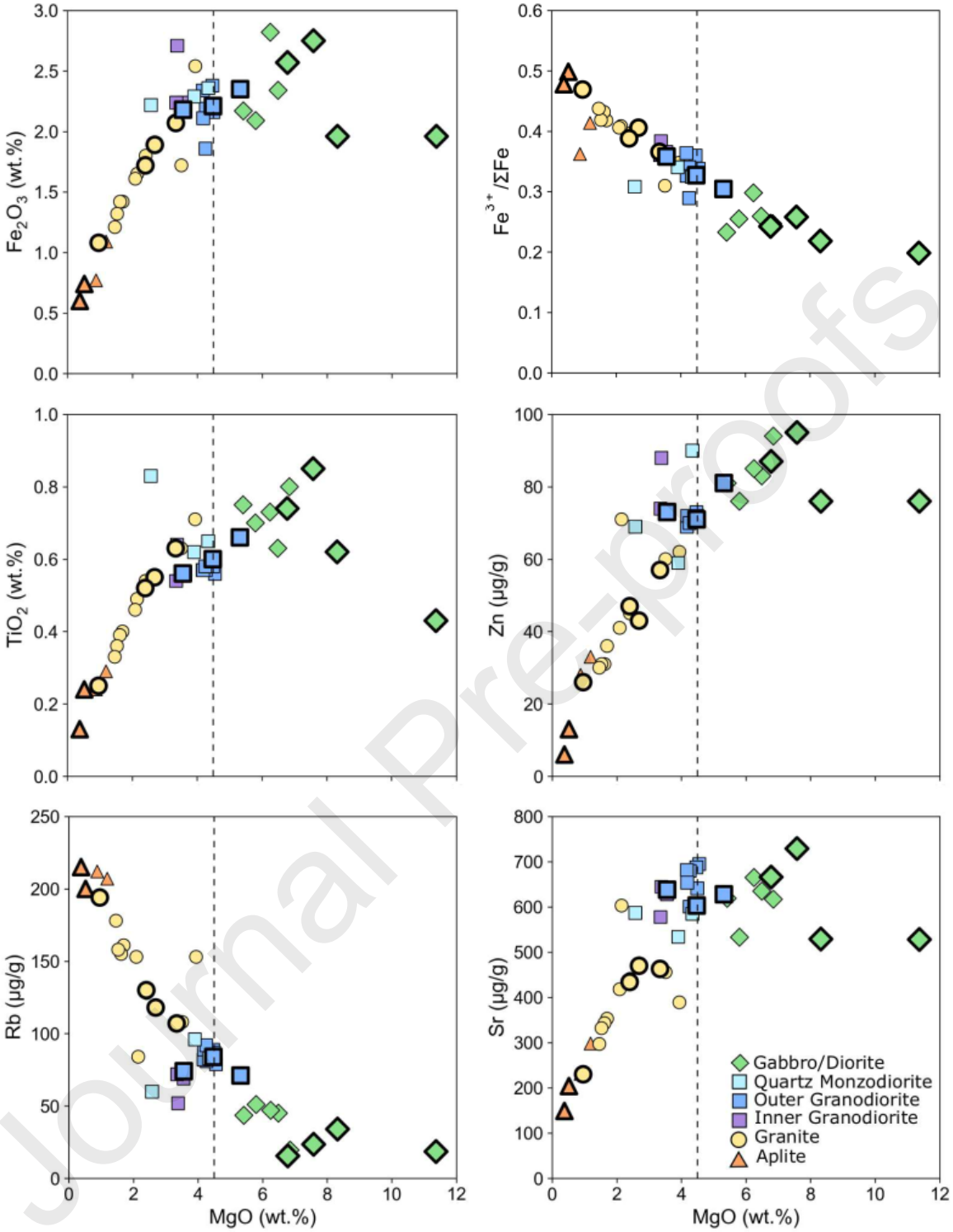

Figure 3

Click here to access/download;Figure;Fig3.pptx

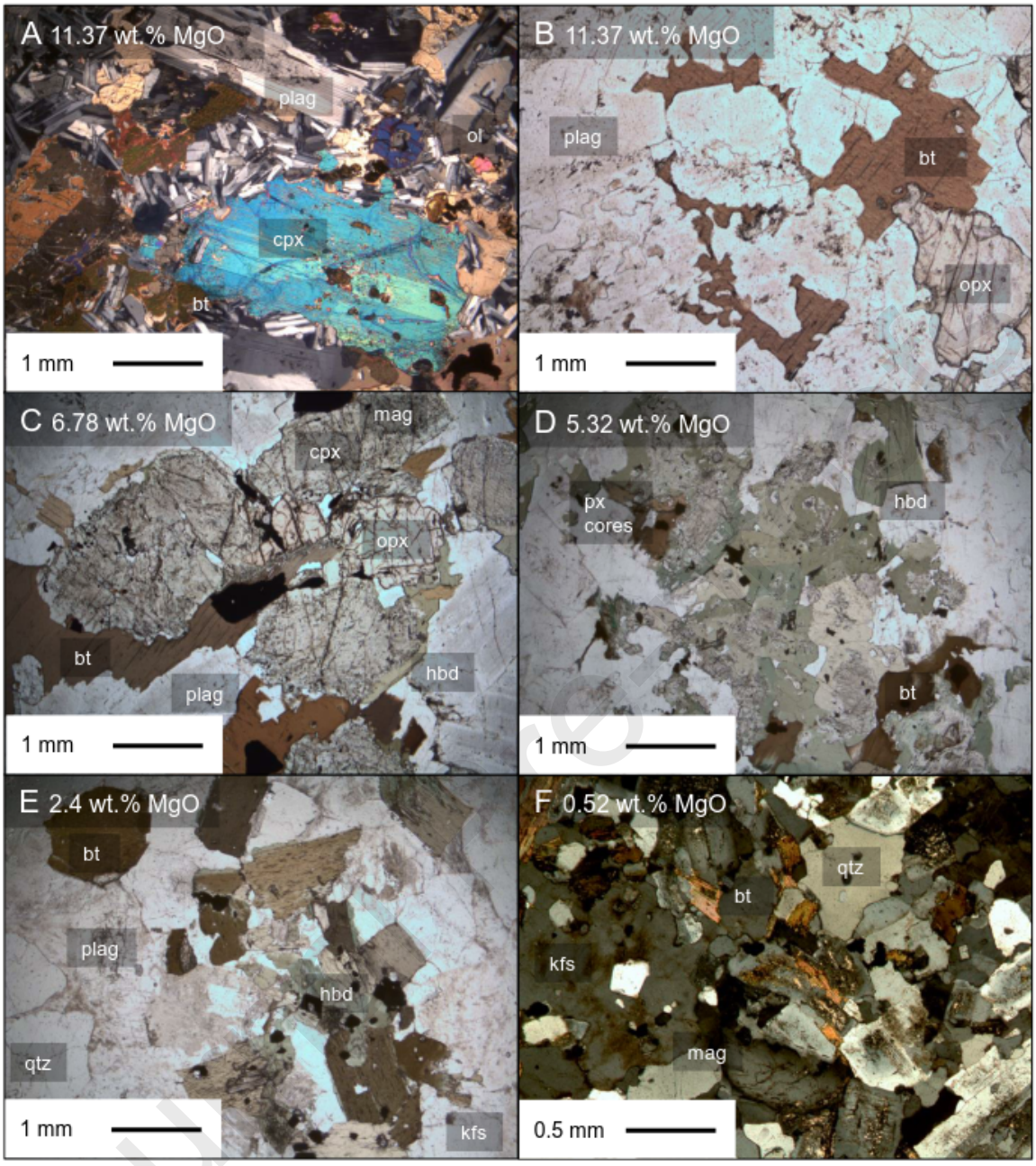

Figure 4

Click here to access/download;Figure;Fig4.pptx

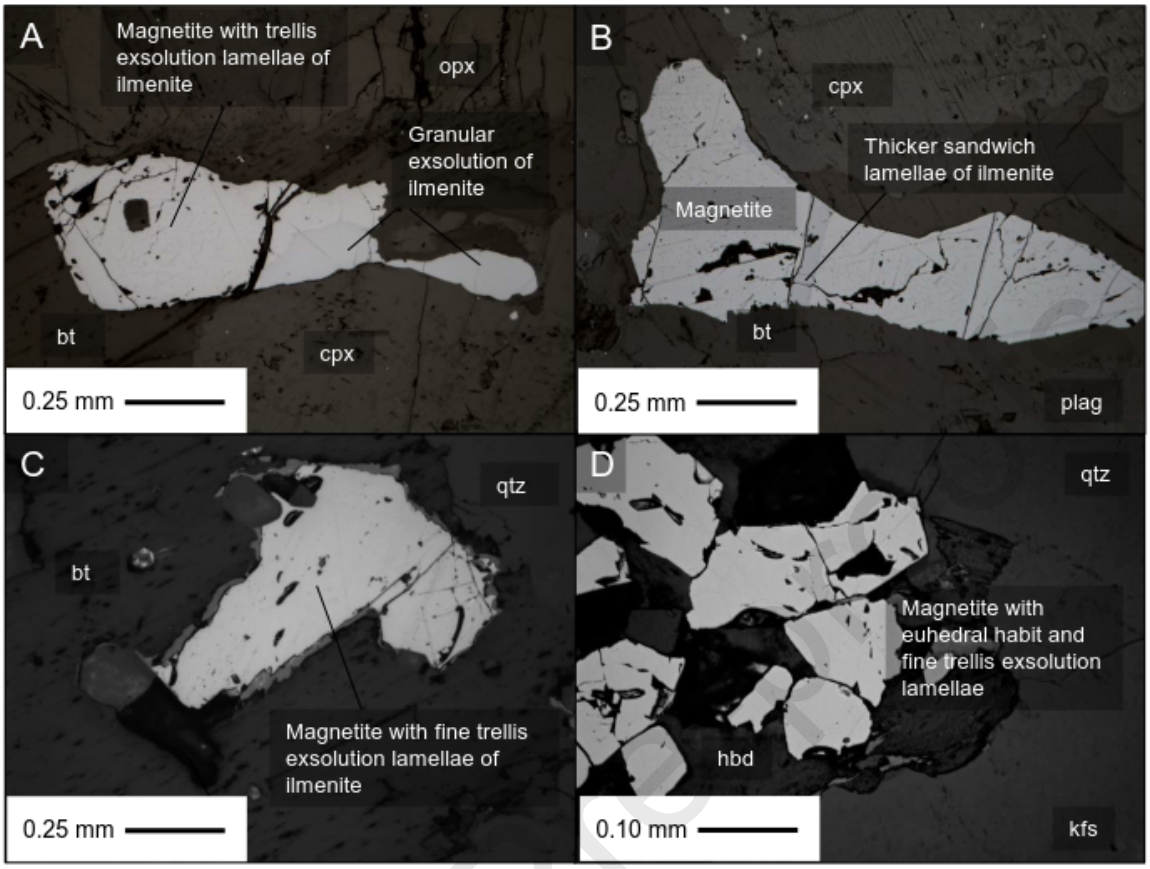

Figure 5

Click here to access/download;Figure;Fig5.eps

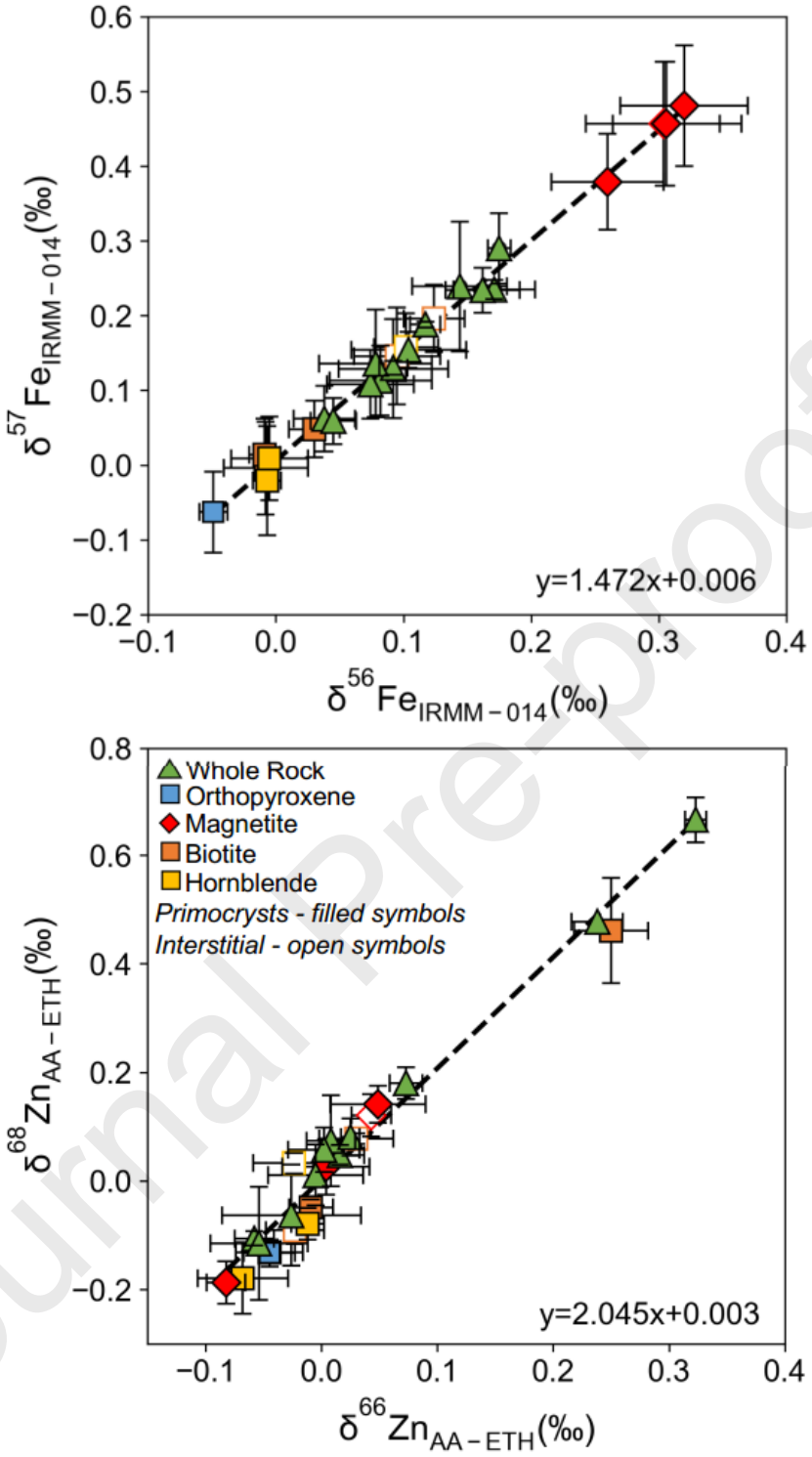

Figure 6

Click here to access/download;Figure;Fig6_Final.eps

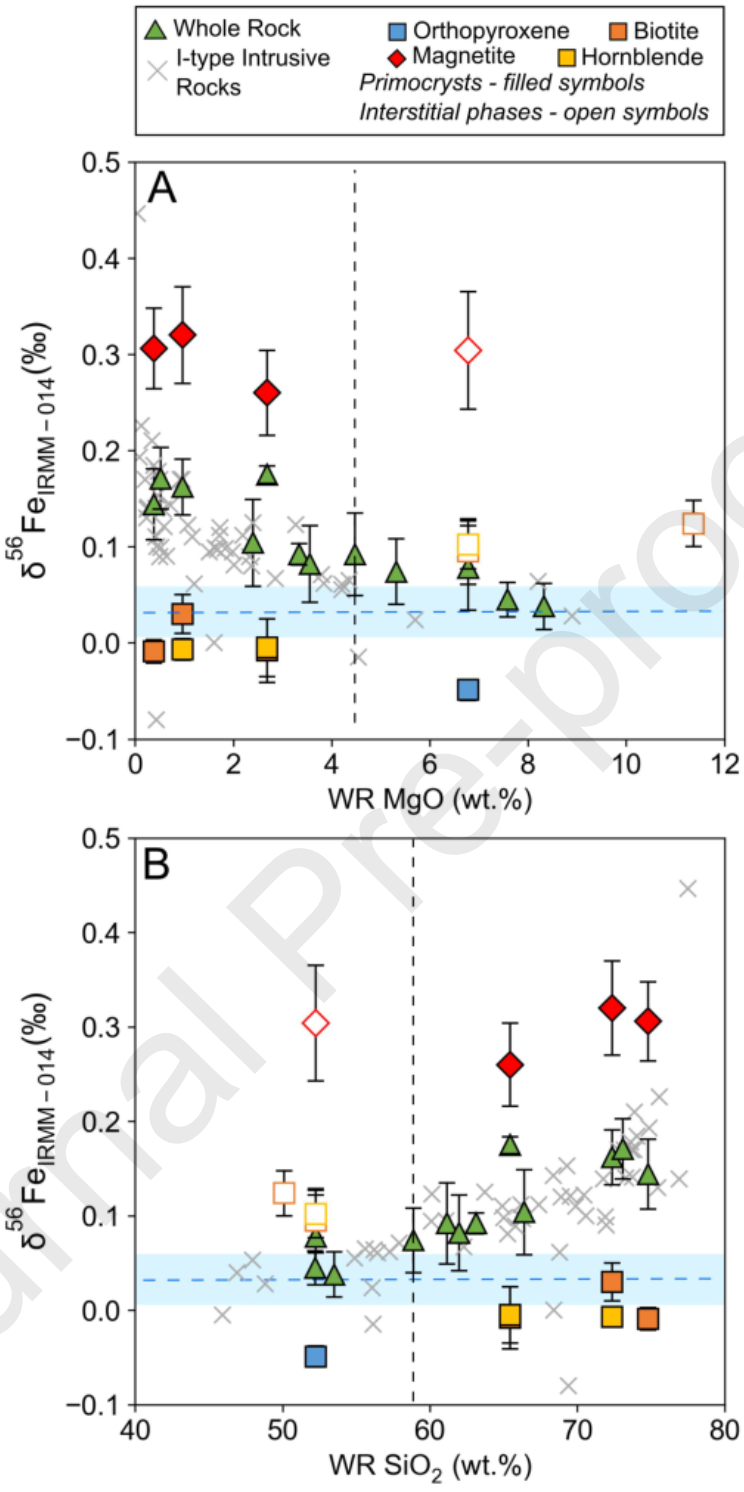

Figure 7

Click here to access/download;Figure;Fig7_Final.eps

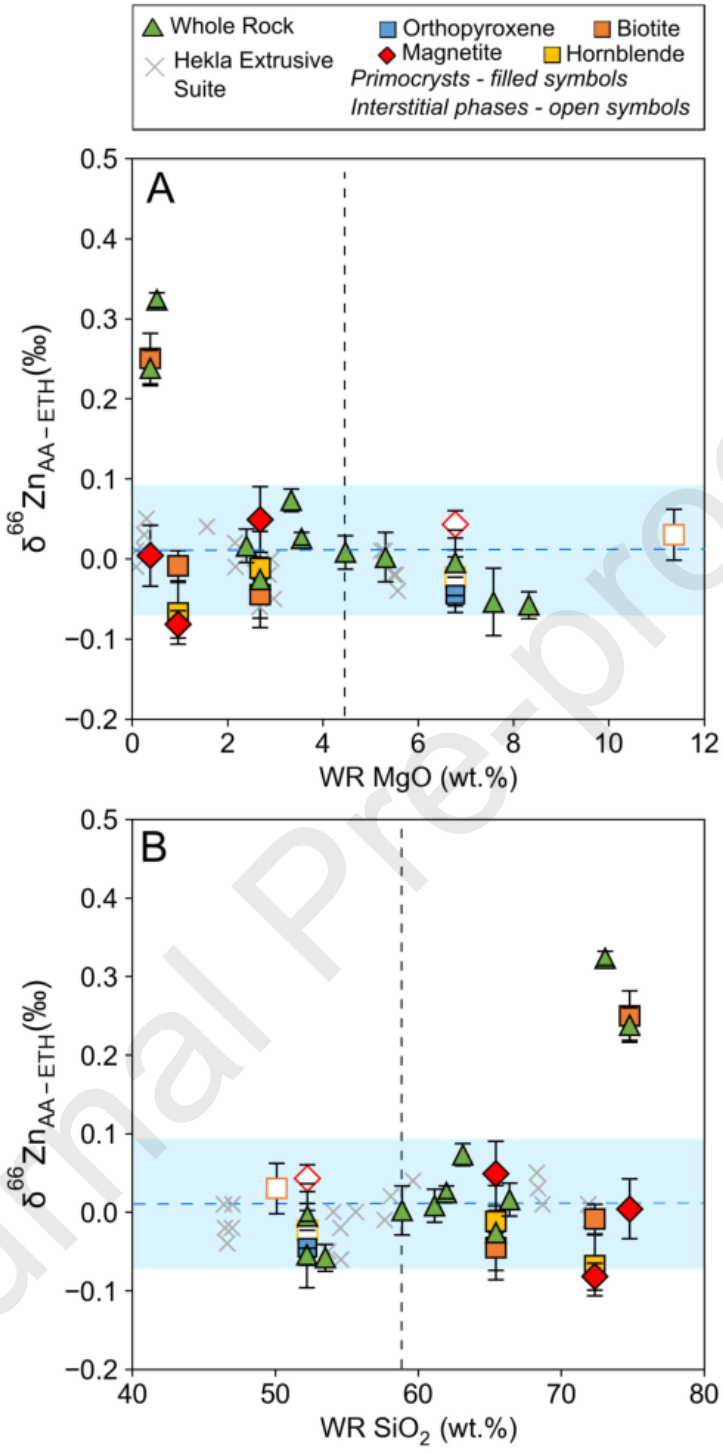

Figure 8

Click here to access/download;Figure;Fig8.eps

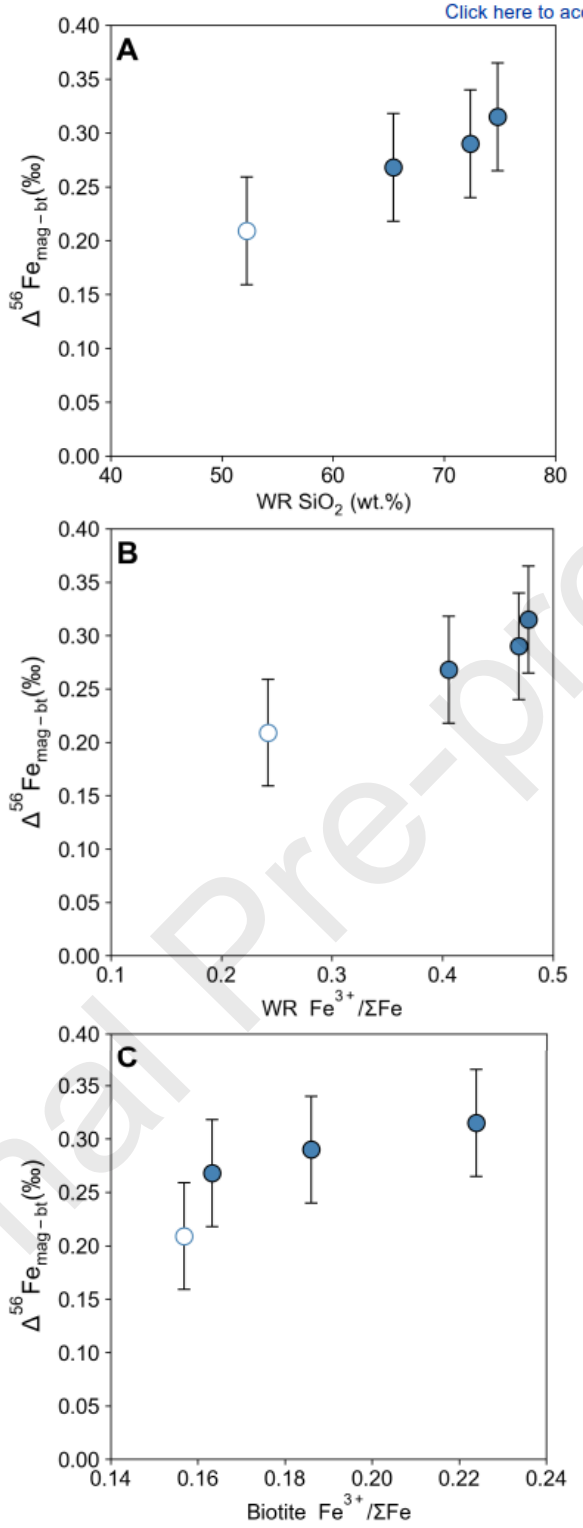

Figure 9

Click here to access/download;Figure;Fig9_Final.eps

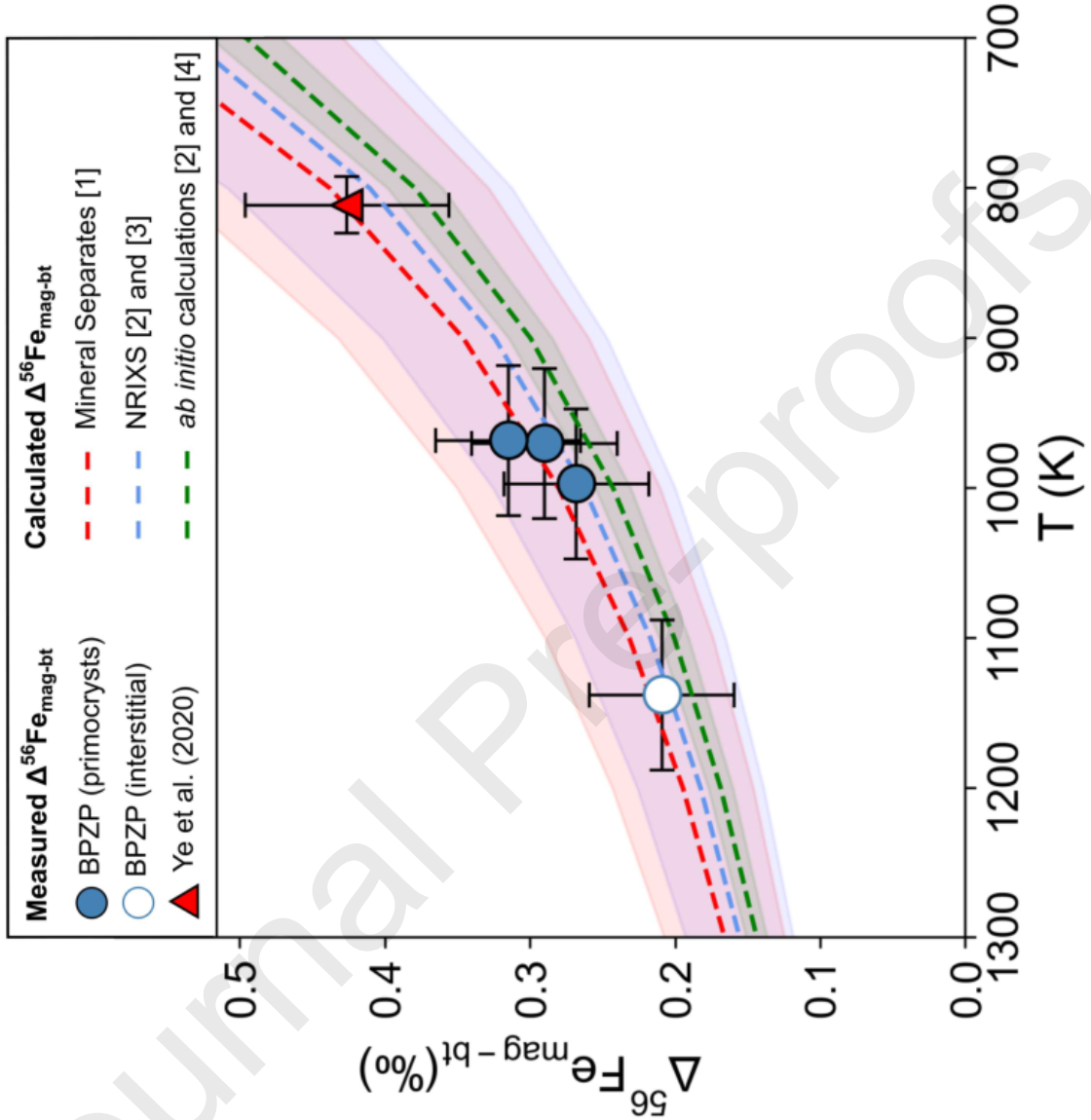

Figure 10

Click here to access/download;Figure;Fig10.eps

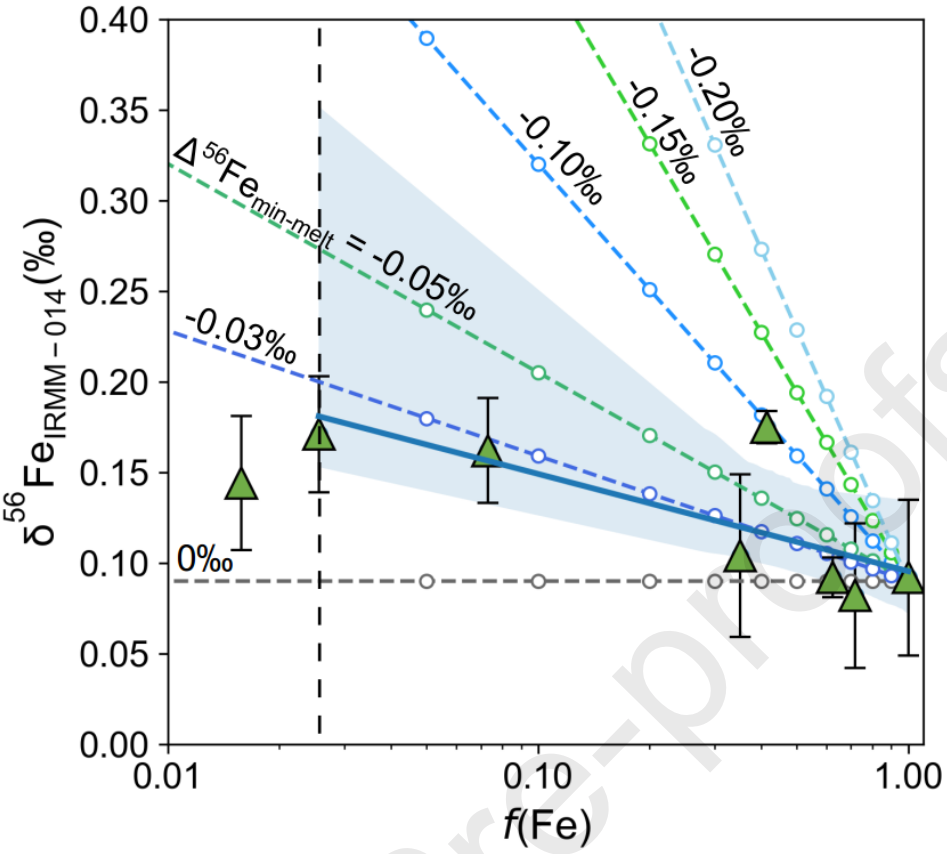

Figure 11

Click here to access/download;Figure;Fig11_New.eps

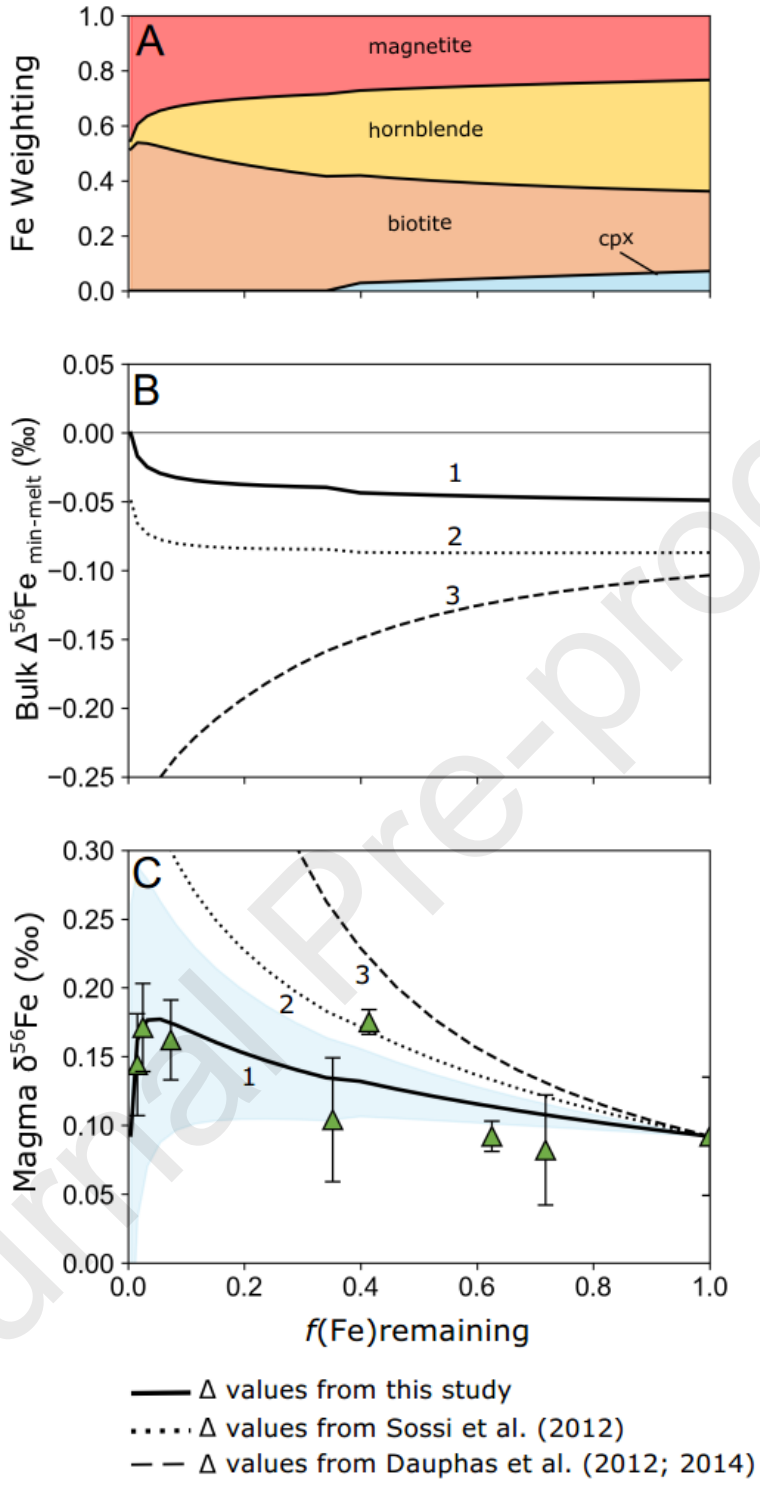

Declaration of interests

☒ The authors declare that they have no known competing financial interests or personal relationships that could have appeared to influence the work reported in this paper.

☐The authors declare the following financial interests/personal relationships which may be considered as potential competing interests: